Journal of Applied Physics

Relaxation volumes of microscopic and mesoscopic irradiation-induced defects in tungsten

Cite as: J. Appl. Phys. **126**, 075112 (2019); https://doi.org/10.1063/1.5094852
Submitted: 06 March 2019 . Accepted: 25 June 2019 . Published Online: 19 August 2019

Daniel R. Mason, Duc Nguyen-Manh, Mihai-Cosmin Marinica, Rebecca Alexander, Andrea E. Sand, and Sergei L. Dudarev

AIP Publishing

Journal of Applied Physics ARTICLE scitation.org/journal/jap

Relaxation volumes of microscopic and mesoscopic irradiation-induced defects in tungsten

Cite as: J. Appl. Phys. **126**, 075112 (2019); doi: 10.1063/1.5094852
Submitted: 6 March 2019 · Accepted: 25 June 2019 ·
Published Online: 19 August 2019

Daniel R. Mason,[1,a)] Duc Nguyen-Manh,[1,2] Mihai-Cosmin Marinica,[3] Rebecca Alexander,[4] Andrea E. Sand,[5] and Sergei L. Dudarev[1,2]

AFFILIATIONS

[1]CCFE, UK Atomic Energy Authority, Culham Science Centre, Oxfordshire OX14 3DB, United Kingdom
[2]Department of Materials, University of Oxford, Parks Road, Oxford OX1 3PH, United Kingdom
[3]DEN-Service de Recherches de Metallurgie Physique, CEA, Universite Paris-Saclay, F-91191 Gif-sur-Yvette, France
[4]Metallurgie Physique et Genie des Materiaux, UMET, CNRS, UMR 8207, Universite de Lille, F-59000 Lille, France
[5]Department of Physics, University of Helsinki, P.O. Box 43, FI-00014 Helsinki, Finland

[a)]**Electronic mail:** daniel.mason@ukaea.uk

ABSTRACT

The low-energy structures of irradiation-induced defects in materials have been studied extensively over several decades, as these determine the available modes by which a defect can diffuse or relax, and how the microstructure of an irradiated material evolves as a function of temperature and time. Consequently, many studies concern the relative energies of possible defect structures, and empirical potentials are commonly fitted to or evaluated with respect to these. But recently [S. L. Dudarev *et al.*, Nucl. Fusion **58**, 126002 (2018)], we have shown that other parameters of defects not directly related to defect energies, namely, their elastic dipole tensors and relaxation volumes, determine the stresses, strains, and swelling of reactor components under irradiation. These elastic properties of defects have received comparatively little attention. In this study, we compute relaxation volumes of irradiation-induced defects in tungsten using empirical potentials and compare to density functional theory results. Different empirical potentials give different results, but some clear potential-independent trends can be identified. We show that the relaxation volume of a small defect cluster can be predicted to within 10% from its point-defect count. For larger defect clusters, we provide empirical fits as a function of defect cluster size. We demonstrate that the relaxation volume associated with a single primary-damage cascade can be estimated from the primary knock-on atom energy. We conclude that while annihilation of defects invariably reduces the total relaxation volume of the cascade debris, there is still no conclusive verdict about whether coalescence of defects reduces or increases the total relaxation volume.

I. INTRODUCTION

Just as it has been long acknowledged that the effect of radiation on materials is inherently multiscale both in time- and spatial-dimensions, so it is accepted that to model these effects requires transfer of high quality data from one model to the next.[1] The form of the data required by a coarse-grained model varies, and a typical workflow in nuclear materials modeling involves finding structural information about individual defects from Density Functional Theory (DFT),[2,3] information about the cascade generation process from Molecular Dynamics (MD),[4–6] and about cascade evolution from object or atomistic Kinetic Monte Carlo (KMC)[7–9] or Cluster Dynamics (CD)[10,11] simulations. This has proved successful for modeling the experimentally observed size and distribution of irradiation-induced defects formed in pure single crystalline materials.[9,12]

Recently, we have shown that it is possible to compute stresses and strains in reactor components on the macroscopic scale of centimeters and meters from the distribution of irradiation-induced defects.[13] As a source term, this model only requires the spatially varying density of relaxation volumes of defects and so allows the

direct simulation of volumetric radiation-induced swelling and the associated stresses from an atomistic or object-based model. At the nanoscale, lattice swelling resulting from the accumulation of radiation defects is experimentally measurable using Micro-Laue diffraction.[14,15] Furthermore, X-ray diffraction measurements show that "negative" lattice strain develops due to the accumulation of vacancies in a material.[16] On a macroscopic scale, predicting the stress state of reactor components arising from irradiation is fundamental to the successful engineering design of a nuclear fission or fusion power plant.[17–19] One outstanding issue, which this paper is intended to address, is to have good quality data for the relaxation volumes of a variety of lattice defects, as while accessible from simulation for years, reporting this information has been somewhat neglected in favor of establishing accurate values of formation energies and low-energy-state structures. For example, a comprehensive compilation of data on relaxation volumes and relaxation volume tensors of individual self-interstitial and vacancy point defects derived from DFT calculations performed for all the bcc metals in the periodic table has been reported only recently.[13,20–22] Data for the relaxation volumes of point defects available prior to these studies were derived mostly from experimental measurements and semiempirical potential calculations[23–27] and exhibited a degree of variability associated with experimental uncertainties or the choice of interatomic interaction potentials. Accurate *ab initio* studies of relaxation volumes of defects mostly involved vacancies in simple or noble metals.[13,25,28–33]

Here, we focus our attention on a single material, tungsten. Tungsten has been chosen as a divertor material for ITER[18,34,35] as it has a high melting point, high thermal conductivity, and high resistance to sputtering. For our purposes, tungsten is also well-suited to this preliminary study of relaxation volumes as it is nearly elastically isotropic[36] at low temperatures. This simplifies the expressions needed for an elastic analysis but is by no means a requirement of the atomistic techniques used here,[20] and the data we present have no assumption of isotropy. The finite temperature calculation of the Helmholtz free energy and an anisotropic elasticity analysis are beyond the scope of the current paper. In Sec. II A, we compute the relaxation volumes of small defect clusters and compare the results obtained with several embedded atom (EAM) potentials with those derived from DFT. In Sec. II B, we move on to larger lattice defect objects. As the number of configurational degrees of freedom becomes very large, we focus on a standard set of idealized dislocation loops and voids, which often form a basis set for object kinetic Monte Carlo (okMC) or Cluster Dynamics (CD) simulations. In Sec. II C, we introduce the orientation-dependent anisotropy of the relaxation. In Sec. II D, we consider interacting groups of defect clusters generated in high-energy collisions simulated by MD. Our goal is to understand the complex-looking stress fields that arise in irradiated metals (see Fig. 1) in terms of the simpler stress fields of their constituent parts, which can then be used to predict volumetric swelling from the output of existing microstructural evolution codes such as okMC or CD.

Early estimates of formation volumes for point defects in tungsten were established by Johnson,[38] using an empirical potential. This work found a negative relaxation volume for a vacancy ($-0.21\Omega_0$, where Ω_0 is the atomic volume) and a positive relaxation volume for the interstitial ($+1.13\Omega_0$). DFT calculations by

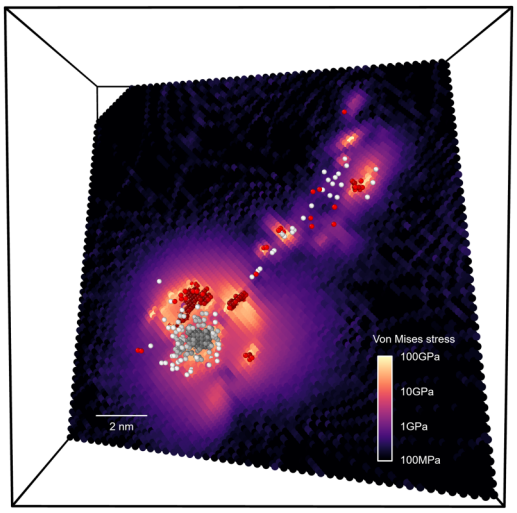

FIG. 1. A typical configuration of defects produced by a collision cascade event in tungsten, initiated by a 150 keV primary knock-on atom (PKA) and simulated using the method described in Sec. II D. Vacancies (white spheres), and interstitials (red), were identified using a Wigner-Seitz defect analysis.[37] The von Mises stress in a [211] plane intersecting the cascade is also shown. Note that close to the defects, the stresses can be as high as 100 GPa, comparable to the shear modulus ($\mu = 160$ GPa). In the study below, we analyze the complex stress fields of individual defects and clusters of defects formed in cascades, similar to those shown in this figure.

Kato *et al.*[39] confirmed the relaxation volume for the vacancy as negative, at $-0.34\Omega_0$, a figure which has since been reproduced several times by independent DFT calculations. The relaxation volume of a $\frac{1}{2}\langle 111\rangle$ interstitial defect was shown to be large and positive in DFT calculations at $+1.68\Omega_0$[15] in a small $4 \times 4 \times 4$ supercell, later confirmed by other DFT calculations.[20,21]

We demonstrate that empirical potentials give varying results for the relaxation volumes of irradiation defects. This is an expected result, as these properties of defects were never originally used as input data during the parameterization of potentials. The relaxation volumes do, however, show systematic trends across potentials. It is beyond the scope of this paper to provide a comprehensive comparison of empirical potentials, instead our comparison will focus on three empirical potentials, which should give an indication of the possible variation.

- The Derlet-Nguyen-Manh-Dudarev (DND) potential[40] has been shown to produce cascade structures that are a good match to experiment.[6,12,41–43]
- One of the four potential parameterizations developed by Marinica *et al.* (CEA-4),[44] which has a good balance between the predicted point- and extended defect properties. This potential was developed from the DND and AM04[45] potentials with additional fitting to the forces on atoms in disordered systems.
- A new potential parameterization by some of the authors (MNB),[46] which is a development of the smooth and

highly-transferable Ackland-Thetford potential,[47,48] corrected to give better properties for vacancy-type structures.

We present simple empirical formulas for the relaxation volumes of defects that might be used for predicting stresses and strains in engineering components containing these defects.[13] As tungsten is (nearly) elastically isotropic, it suffices to present results in terms of a single relaxation volume, and the relaxation volume anisotropy parameter, defined as the ratio of the smallest to largest partial relaxation volumes. Simple formulas are required to switch between this representation and the full dipole tensor for the defect.

Finally, in Sec. III, we compare our results with analytical formulas derived using linear elasticity and surface energies, consider the differences between the empirical potentials used and discuss routes for making predictions for complex microstructures, and in Sec. IV, we compare the predictive power of our results to earlier studies.

II. RELAXATION VOLUME OF DEFECT STRUCTURES

Relaxation volumes can be computed for isolated defects and relaxed cascade configurations using several methods. As a validating convergence study, we compare three methods: the stress method, the cell relaxation method, and the free-surfaces method.

- The stress method. The atom positions are relaxed in a periodic supercell, with the vectors defining the supercell repeat fixed. The stress is computed on each atom and summed to give a single tensor for the cell. The relaxation of a body free from surface tractions due to the defect is predicted from this stress using linear elasticity theory. The lattice vectors of the simulation cell never need to be updated.
- The cell relaxation method. As with the stress method, the atoms are relaxed in a periodic supercell, and the stress is computed. From this a strain is computed, but in contrast to the stress method this is then applied to the supercell, changing its shape and volume. The vectors defining the supercell repeat are updated, and the relaxation process is repeated until convergence, where the macroscopic stress vanishes. This iterative process of relaxing first the atoms and then the cell differentiates this method from the stress method. We note here that there is no *a priori* reason why the minimum energy structure of a defect with one set of lattice vectors is the same as the minimum with a different set.
- The free surface method. A large sphere of atoms is constructed and relaxed, producing a body with explicitly free surfaces.[49] Then, a single defect is constructed inside the sphere, and the entire structure is relaxed again. The volume of a (distorted) spheroid after relaxation is more difficult to compute than with a periodic supercell, as it is not clear where the surface should be drawn. However, the volume enclosed by the convex hull of the atoms V_{hull} is easy to compute using qhull.[50] From this, we can estimate that the volume of the sphere is $V_{\text{spheroid}} = V_{\text{hull}}(R+r)^3/R^3$, where R is the maximum radius of atom positions on the convex hull, and $r = a_0/4$ is one quarter the lattice parameter, which is half the distance between {100} planes in a bcc crystal.[51] We include this nonstandard (and suboptimal) brute-force method as a validation that the linear elasticity approach followed in this work truly predicts the relaxation volume in a body with explicitly free surfaces.

In this work, we do not consider the method of Kanzaki forces[52,53] or the method of matching displacements[54,55] for estimating relaxation volumes using the harmonic region of the crystal only.

To compute the stress due to a defect, and hence the strain in an elastic medium, we compute the dipole tensor as the integrated stress over the cell,[21,56,57]

$$P_{ij} = -\int_V \sigma_{ij}(\mathbf{r})\mathrm{d}^3\mathbf{r}. \tag{1}$$

In an atomistic simulation where the energy is more easily accessible than the stress, we can compute this quantity as the derivative of total energy with respect to a homogeneous body strain,

$$P_{ij} \equiv -\frac{\partial E}{\partial \epsilon^0_{ij}}. \tag{2}$$

The dipole tensor may also be expressed in terms of a symmetric dual tensor, Ω_{kl}, characterizing the volumetric relaxation of the defect and defined by the equation[13,20]

$$P_{ij} \equiv C_{ijkl}\Omega_{kl}, \tag{3}$$

where C_{ijkl} are the elements of the fourth-rank tensor of elastic constants. From this dual tensor, we can find the relaxation volume Ω_{rel} of the defect characterizing the volumetric relaxation of an elastic body free from surface tractions,[56]

$$\Omega_{rel} = \mathrm{Tr}\,\Omega \equiv \sum_{i=1}^{3}\Omega^{(i)}, \tag{4}$$

where $\Omega^{(i)}$ are the three eigenvalues of the tensor Ω_{kl}, corresponding to the three partial relaxation volumes. Hence, we can find the elastic relaxation volume of the defect using a constant-volume calculation, if the elastic constants and dipole tensor of the defect are computed.

For an empirical potential, P_{ij} can be computed simply and analytically. For the embedded-atom form, we compute the energy as a sum over pairwise and many-body contributions: $E = \sum_a V_a + F[\rho_a]$, where $V_a = \frac{1}{2}\sum_b V(r_{ab})$ is a pairwise interaction, $\rho_a = \sum_b \phi(r_{ab})$ models the embedding electron density, and $F[\rho]$ is the many-body embedding energy. The dipole tensor is

$$P_{ij} = -\sum_{a,b}\left(\frac{1}{2}\frac{\partial V}{\partial r}\bigg|_{r_{ab}} + \frac{\partial F}{\partial \rho}\bigg|_{\rho_a}\frac{\partial \phi}{\partial r}\bigg|_{r_{ab}}\right)\frac{r_{ab,i}r_{ab,j}}{r_{ab}}, \tag{5}$$

where r_{ab} is the separation between atoms a and b and $r_{ab,i}$ is its ith Cartesian coordinate. This is a simple sum over atoms and their neighbors, using the same first derivatives as a force calculation

and so is trivially implemented in any MD or atomistic MS code. The (fourth-rank) elastic constant tensor can be computed analytically from the second derivative of energy with respect to strain.[47] The computed elastic constants are given in Table I.

A plot showing the convergence of the numerical procedure for computing the relaxation volume of a 19-interstitial loop with system size is shown in Fig. 2. Extrapolating to infinite system size suggests that all three methods converge to the same result, though at any given finite system size there will be an error, typically scaling as inverse system size $1/n$ (voids relaxed with explicitly free surfaces being an exception, converging as the inverse radius of the free sphere $1/R$). This $1/n$ convergence was also observed recently by Varvenne & Clouet,[55] who attributed this leading error term to the interaction between periodic images. Some indicative data are also given in Table II, proving that the stress method with large supercells is suitable for the structures considered in this work. Relaxation volumes computed with the EAM potentials in this paper are computed using the dipole tensor method at a converged supercell size. Relaxation volumes computed with DFT were computed using the full cell relaxation method.

A. Small defect structures

In this section, we compute the elastic properties of small defect clusters. For sufficiently small clusters, we can perform a fairly comprehensive survey of possible structures and so find the bounds of the variation of the relaxation volumes. The question of which are the most significant set of small clusters to use is rather more difficult. Generally, for a cluster containing N point defects, we might expect to find only a small number of structures within a few millielectronvolts of the ground state. At low temperatures, these are the only ones which need to be considered in equilibrium. But radiation damage is an inherently nonequilibrium process. The system can generally reduce its internal energy by coalescing clusters, and the true equilibrium is only found when nearly all defects have recombined or diffused to sinks. The structures that may actually be found at some time after the cooling of a displacement cascade could therefore be, briefly at least, rather exotic.

Randomly generated interstitial clusters were generated by placing N additional atoms into an otherwise perfect crystal, then relaxing. The extra atoms were placed at random into $[l, m, n]a_0/4$ crystal positions, with $0 \leq lmn < 4$, with the constraint that an atom was not placed if another was already within a distance $a_0/2$. All extra atoms were placed in a central block of $2 \times 2 \times 2$ unit cells. The relaxation volumes as a function of formation energy and cluster size are presented in Fig. 3. We have not put results from CEA4 on this scatter plot. CEA4 has a good deal of structure in its potential, which allows for a very large number of metastable high energy defect clusters to form. In Fig. 3, this would appear as an almost structureless cloud, and we conclude our method of randomly generating interstitial clusters is not suited to this potential.

DFT calculations of small interstitial clusters were performed for this work using the VASP *ab initio* simulation code, using the Projector Augmented Wave (PAW) method[60–62] with semicore electrons included through the use of pseudopotentials. It is important to emphasize that the inclusion of semicore electrons in the valence states has a significant effect on the predicted formation energies of self-interstitial atom (SIA) defects for all the bcc transition metals[2,63,64] and play an important role on the quality of interatomic potential in predicting nonequilibrium properties in tungsten from cascade simulations.[65] Exchange-correlation effects were described using the Perdew-Burke-Ernzerhof generalized gradient approximation.[66] A kinetic energy cutoff of 400 eV was used, with a $3 \times 3 \times 3$ Monkhorst-Pack grid for electron density k-points employed in the case with supercell $(8 \times 8 \times 8)$ calculations $(1024 + N$ atoms, with N up to 22 atoms) for the $\frac{1}{2}\langle 111\rangle$ and $\langle 100\rangle$ interstitial defects. The set of interstitial defect clusters used was the same as in Ref. 67, with the difference that in the earlier work, the energies reported were in the constant-volume approximation, employing the cell size correction by Varvenne *et al.*,[57] whereas here the full cell relaxation method was used. A systematic study of fully-relaxed defect formation volumes for the $\langle 110\rangle$ self-interstitial

TABLE I. The lattice constant a_0 (in angstrom) and elastic constants (in eV/Å^3) of bcc tungsten, from Ref. 15. The surface energies γ_{hkl} of bcc tungsten for the [*hkl*] surface are given in eV/Å^2. The principal surface stresses s_{hkl} for the [*hkl*] surface (two nonzero eigenvalues of $s_{ij} = \gamma\delta_{ij} + \partial\gamma/\partial\epsilon_{ij}$) of bcc tungsten are given in eV/Å^2. The average surface energy γ computed using Eq. (A4), and the average surface stress s using the mean of the principal eigenvalues in Eq. (A4). Experimental elastic constants are from Ref. 58, and surface energy are from Ref. 59.

Method	a_0	c_{11}	c_{12}	c_{44}	$\gamma_{\langle 110\rangle}$	$\gamma_{\langle 100\rangle}$	$\gamma_{\langle 211\rangle}$	$\gamma_{\langle 111\rangle}$	γ
DFT	3.186	3.229	1.224	0.888	0.200	0.245	0.215	0.219	0.229
MNB	3.165 2	3.222	1.263	0.998	0.218	0.239	0.241	0.257	0.234
DND	3.165 2	3.3881	1.304	1.031	0.150	0.187	0.185	0.161	0.174
CEA4	3.143 39	3.265	1.262	1.004	0.157	0.183	0.187	0.201	0.177
Expt	3.165 2	3.324	1.279	1.018					0.229

Method	$s_{\langle 110\rangle}$		$s_{\langle 100\rangle}$		$s_{\langle 211\rangle}$		$s_{\langle 111\rangle}$		s
DFT	0.375	0.253	0.296	0.286	0.465	0.434	0.313	0.313	0.360
MNB	0.330	0.215	0.229	0.229	0.263	0.252	0.215	0.214	0.253
DND	0.150	−0.008	0.291	0.275	0.144	0.044	0.179	0.022	0.129
CEA4	0.125	0.018	0.210	0.210	0.075	0.056	0.064	0.063	0.100

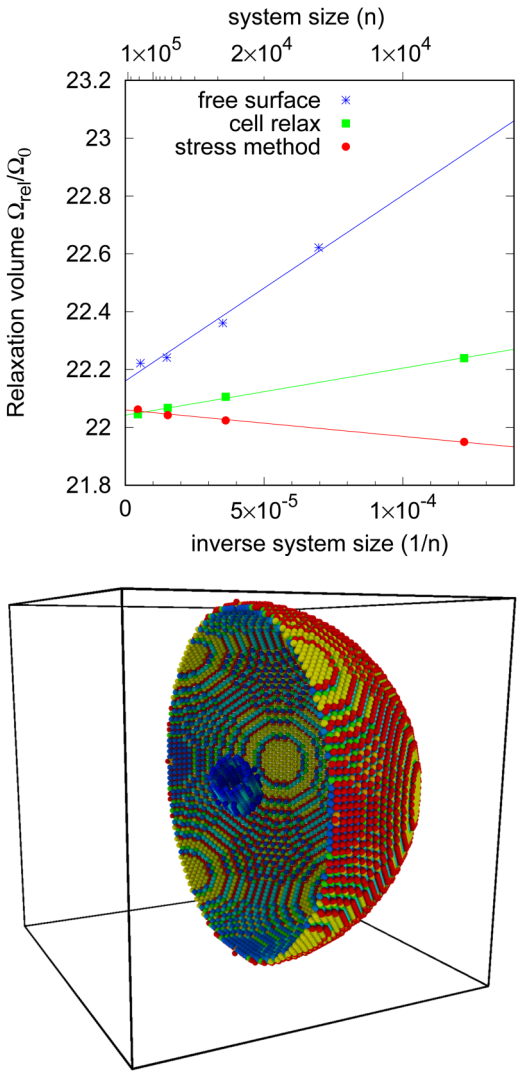

FIG. 2. Above: Example convergence study for relaxation volume of the 19 interstitial cluster computed using three methods. All three methods converge to very similar values, with a system size error inversely proportional to the number of atoms in the simulation cell n. Best fit lines are indicated to guide the eye. Calculations were performed with the MNB potential. Other potentials and other defects show qualitatively similar results. Below: Geometry used for free-surface calculations. An unsupported free sphere of atoms was constructed and relaxed, then a single defect was generated in the center, and the atoms relaxed again. The volume before and after the defect was placed was computed using qhull.[50] One half of the sphere is shown,[37] together with high-energy atoms of the defect. Atoms are colored by excess potential energy from 0 eV (blue) to 2 eV (red). Atoms with energy under 0.1 eV are not shown. In this image, a 55 interstitial loop is embedded in a sphere of 180 000 atoms and relaxed with the MNB potential.

clusters within the underlying three-dimensional C15 Laves phase structure[68] was also performed. The small C15 interstitial clusters in the bcc lattice of iron are known to be highly stable in a comparison with $\frac{1}{2}\langle 111\rangle$ self-interstitial defect clusters due to magnetic

TABLE II. Relaxation volumes for vacancy defects (monovacancy and 15, 65, and 259 vacancy spheres) and interstitial defects ($1/2\langle 111\rangle$ dumbbell and 19, 55, and 199 $\langle 111\rangle$ interstitial loops). The volumes are expressed in units of atomic volume, computed using the MNB potential. The cell relaxation and stress method calculations used a $48 \times 48 \times 48$ unit cell supercell. The free surfaces method used a sphere with an initial radius of 28 unit cells. It is clear that the stress method does indeed reproduce the relaxation volume of the defect in a body with traction free surfaces at large system size and so is an acceptable faster alternative to the full cell relaxation calculation.

	Cell relaxation	Stress method	Free surfaces
1v	−0.367	−0.368	−0.350
$15v_{sph}$	−3.599	−3.625	−3.731
$65v_{sph}$	−9.658	−9.760	−10.351
$259v_{sph}$	−21.634	−21.806	−24.291
$1i_{\langle 111\rangle}$	1.399	1.400	1.415
$19i_{\langle 111\rangle}$	22.045	22.062	22.222
$55i_{\langle 111\rangle}$	60.325	60.250	60.705

effects. Here, we include them for completeness, as their formation energy compared to interstitial loops may be affected by the applied strain.[69]

Randomly generated vacancy clusters were produced by removing atoms on a random path through an otherwise perfect crystal. The path was allowed to move in $\langle 111\rangle$ and $\langle 100\rangle$ directions and allowed to overlap itself. A path of length L steps leads to $\leq L$ vacancies placed in a loose cluster. These vacancy clusters were then relaxed and the lowest energy structures were passed to DFT for a comparison calculation. It is important to emphasize that in the present DFT calculations for both SIA and vacancy clusters, the

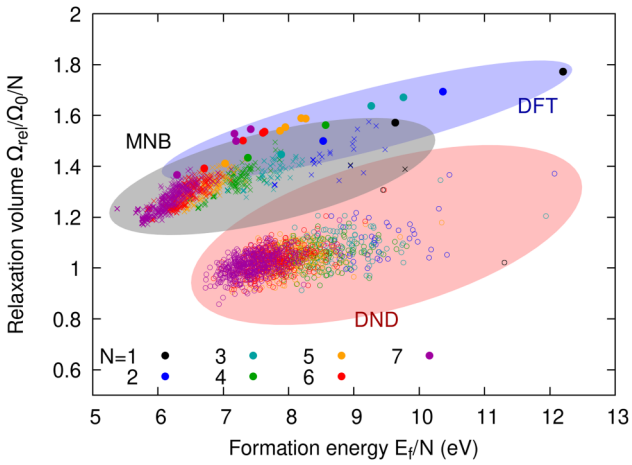

FIG. 3. Relaxation volumes of randomly generated interstitial defect clusters for different numbers of interstitial atoms in the defect, N. DFT values for energies and relaxation volumes from Ref. 13 are shown with filled circles. Crosses: the values computed with MNB potential; open circles are the values computed using the DND potential. Shaded ellipses are drawn to guide the eye to the regions covered by data generated using the relevant potentials. Note that the DND potential tends to predict a higher formation energy and lower relaxation volume of a defect cluster than the MNB potential.

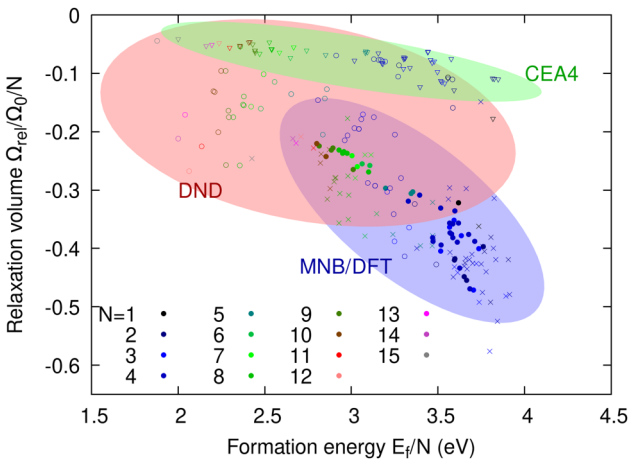

FIG. 4. Relaxation volumes of randomly generated vacancy defect clusters for different numbers of vacant sites in the defect, *N*. DFT values for energies are from Ref. 46, the relaxation volumes were computed in this study and are shown with filled circles. Crosses: the values computed with MNB potential; open circles with DND potential. Shaded ellipses are drawn to guide the eye to the regions covered by the potentials. Note that the DND potential tends to predict a lower formation energy and smaller magnitude relaxation volume than the MNB potential. The CEA potential predicts the smallest relaxation volume. The MNB potential data have a high degree of overlap with the DFT relaxation volume data.

full cell relaxation method has been adopted to investigate the relaxation volume of defect structures. Details of the DFT calculations can be found in Ref. 46. Results are shown in Fig. 4.

The slab model including a 18 Å vacuum layer between the top and bottom surfaces has been employed for calculations of W (100), W(110), W(111), and W(211) surface energies, where 15, 15, 24, and 24 atomic layers were used, respectively, to ensure DFT convergence.

Two trends are immediately apparent in Figs. 3 and 4. Firstly, we see that larger clusters have a lower formation energy per point defect. This is just an illustration of the reduction in energy due to coalescence of individual point defects into a cluster of defects, but we also can see that the magnitude of the relaxation volume reduces with cluster size. By coalescing, the volume strain on the lattice required to accommodate small defects is reduced.

The second trend we see is that the distribution of relaxation volumes is small, of order ± 0.1 atomic volume per point defect, despite the random nature of the defect cluster generation.

A visually striking consequence of this is that the scatter plots for different potentials do not significantly overlap, but this is of limited physical significance as the offset for each potential is a consequence of its fitting, and the fitting did not consider relaxation volume.

The true physical significance of this result is that even if the exact structure of a defect cluster is not known, its relaxation volume can often be estimated from the number of point defects that it contains. The accuracy in the estimate of the relaxation volume may be rather low, as the different potentials given different offsets, but this lack of accuracy will itself be small compared to the current accuracy in modeling the time-dependent evolution of cascades.

Tabulated values of the relaxation volumes of low-energy small defect clusters are given in Table III.

B. Lowest energy defect structures

Having considered randomly generated defect clusters, we now turn our attention to larger low-energy defects. Experimentally, both the $\langle 100 \rangle$ and $\frac{1}{2}\langle 111 \rangle$ interstitial and vacancy-type loops are observed in ion-irradiated ultrahigh purity tungsten foil in TEM.[9,70] We will consider these four loop types as idealized, planar, circular, and prismatic loops, and they might be the basis set for time-evolution in object kMC or CD. To these objects, we add the spherical voids. It may be that, especially at larger sizes, the facetted voids, or hexagonal prismatic loops, have slightly lower energy.[71,72] For our purposes, it is not necessary to guarantee that we have the true ground state of a defect cluster as we are attempting to find trends that govern the variation in the relaxation

TABLE III. The relaxation volumes (Ω_{rel}/Ω_0) of the lowest energy vacancy and interstitial clusters containing *N* point defects, $1 \leq N \leq 7$. These relaxation volumes were computed using full relaxation of the simulation cell and atom positions.

		Ω_{rel}/Ω_0						
Method	Character	$N = 1$	2	3	4	5	6	7
DFT	Vacancy	−0.32	−0.84	−1.21	−1.28	−1.48	−1.53	−1.69
MNB	Vacancy	−0.36	−0.85	−1.29	−1.60	−1.88	−2.27	−1.96
DND	Vacancy	−0.11	−0.17	−0.51	−0.58	−0.68	−0.96	−1.10
CEA4	Vacancy	−0.18	−0.22	−0.28	−0.32	−0.35	−0.45	−0.46
DFT	i⟨111⟩	1.57	3.00	4.34	5.73	7.06	8.35	9.56
MNB	i⟨111⟩	1.40	2.65	3.92	5.08	6.25	7.39	8.63
DND	i⟨111⟩	1.31	2.41	3.48	3.85	4.53	5.76	6.45
CEA4	i⟨111⟩	1.25	2.38	4.57	4.80	6.06	7.36	6.97
DFT	i⟨100⟩	1.77	3.39	4.91	6.25	7.77	9.00	10.70
DFT	i C15		3.92		6.59	8.19	9.37	11.00

volume, independent of the choice of interatomic interaction potential.

We construct the prismatic loops and spherical voids using the procedure proposed in Ref. 73. Formation energies and relaxation volumes for the interstitial defects are presented in Fig. 5 and for vacancy defects in Fig. 6. The formation energies are included here as a comparison to previous studies and to provide a complete empirically parameterized data set for future multiscale modeling studies. We find that our answers agree with the results given in Refs. 72 and 73 to order of the symbol size.

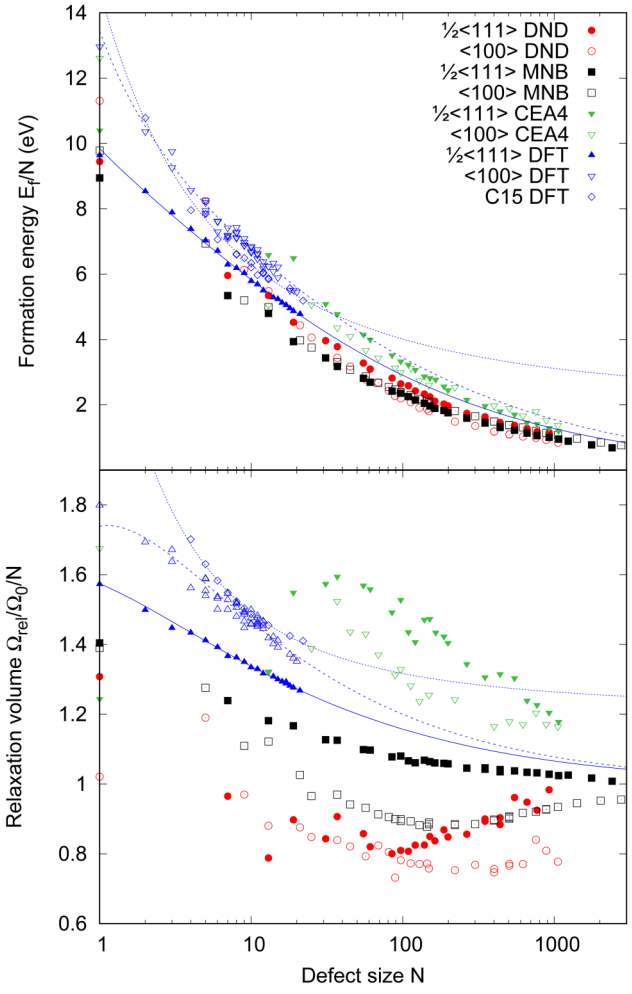

FIG. 5. Formation energy and relaxation volume of low-energy interstitial defect clusters. All clusters and loops are of circular shape. DFT values for formation energies are extrapolated with lines fitted to $E_f = a_0\sqrt{N}\ln N + a_1\sqrt{N} + a_2$ (see Table IV). DFT values for relaxation volumes are extrapolated with lines fitted to $|\Omega_{rel}/\Omega_0| = N + b_0\sqrt{N}\ln N + b_1\sqrt{N} + b_2$ (see Table V). Note that the energies for ideal interstitial defects computed with the potentials are very similar, but the relaxation volumes differ considerably with the DND potential typically predicting smaller values and CEA4 larger.

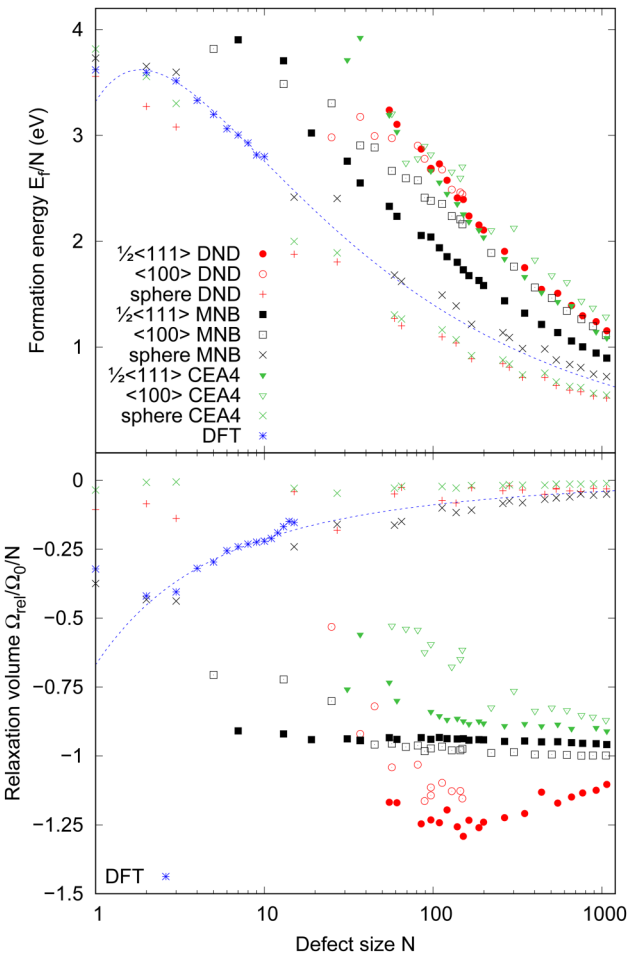

FIG. 6. Formation energy and relaxation volumes of low-energy vacancy defect clusters. The loops were generated with circular shapes, and the voids as spheres. DFT computed energies of the low-energy vacancy clusters from Ref. 46, with an extrapolated line fitted to $E_f = a_0 N^{2/3} + a_1$. DFT computed relaxation volumes for the same structures in Ref. 46 fitted to $\Omega_{rel}/\Omega_0 = b_0 N^{2/3} + b_1$.

We can see from Fig. 5 that the relaxation volume of a large interstitial loop tends to $\lim_{N\to\infty} \Omega_{rel}/\Omega_0 = N$, where Ω_0 is the atomic volume. This result confirms that the volume per atom in an edge dislocation, which is a semi-infinite plane of atoms embedded in a crystal lattice, must be Ω_0. What is more surprising is the slow rate at which the result converges to this answer. Though the vertical scale in Fig. 5 is chosen to exaggerate the effect, nevertheless, it can be that loops need to be well over 100 point defects, perhaps even over 1000 before this limit can truly be said to be reached. To give the reader an idea of the spatial scale involved, a circular $\frac{1}{2}\langle 111\rangle$ dislocation loop containing 1000 interstitials has the diameter of 8.5 nm. A second interesting feature of Fig. 5 is that the relaxation volume is not necessarily a monotonic function of the number of interstitial atoms N.

TABLE IV. Linear regression fits for the formation energy (in electronvolts) of interstitial and vacancy loops fitted to the form $E_f = a_0\sqrt{N}\ln N + a_1\sqrt{N} + a_2$. The DFT values shown are from this study using the cell relaxation method. Note that the fits should only be considered accurate in the ranges covered by the points in Figs. 5 and 6.

Method	Structure	a_0	a_1	a_2
DFT	i⟨111⟩	4.838 ± 0.039	6.18 ± 0.17	3.62 ± 0.23
DFT	i⟨100⟩	6.021 ± 0.032	4.76 ± 0.13	8.23 ± 0.17
MNB	i⟨111⟩	3.394 ± 0.007	7.081 ± 0.052	1.80 ± 0.16
MNB	i⟨100⟩	4.773 ± 0.018	1.10 ± 0.13	9.76 ± 0.36
MNB	v⟨111⟩	4.155 ± 0.016	−0.01 ± 0.12	6.03 ± 0.38
MNB	v⟨100⟩	5.588 ± 0.034	−2.27 ± 0.25	3.20 ± 0.84
DND	i⟨111⟩	3.456 ± 0.025	10.11 ± 0.17	−0.74 ± 0.50
DND	i⟨100⟩	1.479 ± 0.036	15.87 ± 0.25	−3.32 ± 0.69
DND	v⟨111⟩	4.684 ± 0.079	5.05 ± 0.60	2.82 ± 2.5
DND	v⟨100⟩	4.01 ± 0.28	15.0 ± 1.8	−64.6 ± 4.9
CEA4	i⟨111⟩	2.706 ± 0.033	21.55 ± 0.23	−11.31 ± 0.71
CEA4	i⟨100⟩	7.149 ± 0.080	−3.33 ± 0.53	16.12 ± 1.6
CEA4	v⟨111⟩	4.675 ± 0.075	3.08 ± 0.54	15.17 ± 1.9
CEA4	v⟨100⟩	1.99 ± 0.22	31.4 ± 1.7	−126.3 ± 6.7

A regression analysis of the relaxation volume as a function of size for interstitial loops suggests that an excellent fit can be found for the empirical form

$$\Omega_{rel}/\Omega_0 = N + b_0\sqrt{N}\ln N + b_1\sqrt{N} + b_2. \quad (6)$$

We fit this using least squares fitting to $(\Omega_{rel}/\Omega_0 - N)/\sqrt{N}$ and find error bar estimates using bootstrapping.[74] Fits for the relaxation volumes and formation energies are given in Tables IV and V, respectively. Formation energies have been fitted to $E_f/\sqrt{N}$ using the same least squares method.

In Fig. 6, we see that the relaxation volume of a large vacancy loop tends to $\lim_{N\to\infty}\Omega_{rel}/\Omega_0 = -N$ and again may be nonmonotonic. At small cluster sizes $N < 30$, however, it is not clear if there should be a single function describing the relation between the relaxation volume and point defect count N. Small vacancy loops are unstable with respect to their transformation to open platelets[73] and subsequently to spherical voids, particularly for the DND and CEA-4 potentials, so the smallest relaxed vacancy clusters may not be strictly classified as "loops." We have omitted small vacancy clusters that show significantly different elastic properties to large loops.

A regression analysis of relaxation volume and formation energy of the C15 structures computed using DFT are tabulated in Table VI. The formation energy is fitted to $E_f = a_0N + a_1N^{2/3} + a_2$, indicating that the energy is driven by both volume and surface energy terms. The relaxation volume is well fitted by this same form, $\Omega_{rel}/\Omega_0 = b_0N + b_1N^{2/3} + b_2$. It is not required that the relaxation volume per C15 interstitial tends to

TABLE V. Linear regression fits for the relaxation volume (Ω_{rel}/Ω_0) of interstitial and vacancy loops fitted to the form $\Omega_{rel}/\Omega_0 = \pm N + b_0\sqrt{N}\ln N + b_1\sqrt{N} + b_2$, where the positive and negative signs are for interstitial and vacancy loops, respectively. Note that the fits should only be considered accurate in the ranges covered by the points in Figs. 5 and 6.

Method	Structure	b_0	b_1	b_2
DFT	i⟨111⟩	−1.983 ± 0.007	2.614 ± 0.026	−3.195 ± 0.035
DFT	i⟨100⟩	−1.977 ± 0.003	2.698 ± 0.011	−3.330 ± 0.015
MNB	i⟨111⟩	0.008 ± 0.002	0.738 ± 0.010	−0.179 ± 0.021
MNB	i⟨100⟩	−0.420 ± 0.007	0.622 ± 0.048	2.13 ± 0.16
MNB	v⟨111⟩	0.253 ± 0.002	−0.480 ± 0.008	
MNB	v⟨100⟩	−0.155 ± 0.003	1.053 ± 0.015	
DND	i⟨111⟩	−0.061 ± 0.016	−1.566 ± 0.096	2.95 ± 0.23
DND	i⟨100⟩	−1.348 ± 0.006	3.534 ± 0.032	
DND	v⟨111⟩	0.112 ± 0.009	−5.462 ± 0.055	25.07 ± 0.26
DND	v⟨100⟩	0.377 ± 0.081	−6.83 ± 0.49	39.43 ± 1.22
CEA4	i⟨111⟩	−0.050 ± 0.018	7.44 ± 0.12	−22.20 ± 0.32
CEA4	i⟨100⟩	0.845 ± 0.027	−0.94 ± 0.17	1.60 ± 0.44
CEA4	v⟨111⟩	0.384 ± 0.015	−0.19 ± 0.10	2.08 ± 0.33
CEA4	v⟨100⟩	0.554 ± 0.041	−0.14 ± 0.32	13.9 ± 1.2

TABLE VI. Linear regression fits for the formation energy (in electronvolts) and relaxation volume Ω_{rel}/Ω_0 of interstitial clusters in the C15 structure. Relaxation volume are fitted to $\Omega_{rel}/\Omega_0 = b_0N + b_1N^{2/3} + b_2$. The structures taken were those used in Ref. 67, using the cell relaxation method, with sizes $2 \leq N \leq 22$. Energies are fitted to $E_f = a_0N + a_1N^{2/3} + a_2$, as suggested by Ref. 67, indicating terms dependent on volume and surface area.

Method	a_0	a_1	a_2	b_0	b_1	b_2
DFT	2.37 ± 0.06	7.39 ± 0.20	4.92 ± 0.29	1.22 ± 0.01	0.39 ± 0.03	0.87 ± 0.04

$\lim_{N\to\infty} \Omega_{rel}/\Omega_0 = N$, as the structure is not bcc. We note that the C15 structures are higher energy than the $\frac{1}{2}\langle 111\rangle$ interstitial dislocation loops. Our fitting suggests that at larger defect sizes C15 will be less stable than dislocation loops.

A regression analysis of relaxation volume and formation energy of voids are tabulated in Table VII. A regression analysis of the relaxation volume of a void as a function of void size suggests that an excellent fit can be found for the form $\Omega_{rel}/\Omega_0 = b_0N^{2/3} + b_1$, for $N > 5$. The two-thirds power implies that the elastic relaxation of a void is driven by the minimization of the surface energy of the void, and the resulting elastic contraction of the material around it. Results for the relaxation volumes are given in Table VII, and the DFT fit is shown in Fig. 6. The MNB potential predictions are in excellent agreement with the DFT results for the relaxation volume. The relaxation volumes of the lowest energy vacancy clusters for $1 \leq N \leq 7$ are given in Table III. We analyze the relaxation volume of the void using linear elasticity theory in Sec. III B. The formation energy in Table VII is fitted to $E_f = a_0N^{2/3} + a_1$, indicating that the energy is driven by surface energy alone.

C. The anisotropy of the elastic relaxation

In Eq. (4), we expressed the total relaxation volume as the sum of the three partial relaxation volumes. These three partial volumes, plus the corresponding eigenvectors, completely specify the tensor Ω_{kl}, and hence the dipole tensor through Eq. (3).

For cubic crystals, it is straightforward to invert the matrix equations and recover the dipole tensor. For the perfect defect cluster shapes considered in Sec. II B, one eigenvector describes both the Burgers vector and normal of the loops, and so this task can be accomplished simply and analytically.

For a $\mathbf{b} = \frac{1}{2}[111]$ loop with the {111} habit plane (as is the lowest energy case in tungsten), the dipole tensor has the general form

$$P_{\frac{1}{2}[111]} = \begin{pmatrix} a & b & b \\ b & a & b \\ b & b & a \end{pmatrix}, \tag{7}$$

where a and b are numerical parameters with units of energy. The dipole tensor for other symmetry related $\frac{1}{2}\langle 111\rangle$ loops is found by taking negative signs in the off-diagonal elements as appropriate. In a cubic crystal, we can readily find the elastic compliance tensor ($S \equiv C^{-1}$). Its representation as a matrix in the Voigt notation has the simple form

$$S = \begin{pmatrix} \frac{c_{11}+c_{12}}{d} & \frac{-c_{12}}{d} & \frac{-c_{12}}{d} & 0 & 0 & 0 \\ \frac{-c_{12}}{d} & \frac{c_{11}+c_{12}}{d} & \frac{-c_{12}}{d} & 0 & 0 & 0 \\ \frac{-c_{12}}{d} & \frac{-c_{12}}{d} & \frac{c_{11}+c_{12}}{d} & 0 & 0 & 0 \\ 0 & 0 & 0 & \frac{1}{c_{44}} & 0 & 0 \\ 0 & 0 & 0 & 0 & \frac{1}{c_{44}} & 0 \\ 0 & 0 & 0 & 0 & 0 & \frac{1}{c_{44}} \end{pmatrix}, \tag{8}$$

with $d = c_{11}^2 + c_{11}c_{12} - 2c_{12}^2$, and hence, using Eq. (3) for tensor Ω_{kl}, we find the partial relaxation volumes

$$\begin{aligned} \Omega^{(1)} = \Omega^{(2)} &= \frac{a}{c_{11}+2c_{12}} - \frac{b}{c_{44}}, \\ \Omega^{(3)} &= \frac{a}{c_{11}+2c_{12}} + 2\frac{b}{c_{44}}. \end{aligned} \tag{9}$$

We can define a single dimensionless measure of the anisotropy of relaxation for the structures considered here as a ratio of

TABLE VII. Linear regression fits for the formation energy (in electronvolts) and relaxation volume Ω_{rel}/Ω_0 of vacancy clusters and voids. The energy is fitted to the form $E_f = a_0N^{23} + a_1$, indicating a domination by surface energy. The relaxation volume is fitted to the form $\Omega_{rel}/\Omega_0 = b_0N^{2/3} + b_1$, indicating this too is driven by surface energy. The DFT data use the lowest energy structures for $1 \leq N \leq 10$; the EAM data use the lowest energy structures for $6 \leq N \leq 10$ and spherical voids for $15 \leq N \leq 1067$.

Method	a_0	a_1	b_0	b_1
DFT	7.18 ± 0.05	−7.72 ± 0.16	−0.49 ± 0.04	−0.23 ± 0.13
MNB	7.35 ± 0.06	−7.4 ± 3.0	−0.50 ± 0.01	−0.77 ± 0.40
DND	5.25 ± 0.05	−1.9 ± 2.3	−0.31 ± 0.02	0.3 ± 1.1
CEA4	5.56 ± 0.06	−3.2 ± 2.8	−0.122 ± 0.003	0.10 ± 0.12

the smallest to largest (magnitude) partial relaxation volumes,

$$\alpha \equiv \frac{\Omega^{(1)}}{\Omega^{(3)}}. \tag{10}$$

The value $\alpha = 1$ indicates that all the three partial relaxation volumes are equal, as should be the case for a spherical void. A value in the interval $0 < \alpha < 1$ indicates that the principal lattice relaxation is along the Burgers vector, but there are also smaller relaxations in the two orthogonal directions with the same sign (i.e., compressive or tensile) as the principal relaxation. The value $\alpha = 0$ indicates that the only lattice relaxation is along the Burgers vector. A value $\alpha < 0$ indicates that the principal lattice relaxation is along the Burgers vector, but there are also smaller relaxations in the two orthogonal directions with the opposite sign (i.e., compressive or tensile) as the principal relaxation.

For a $\frac{1}{2}\langle 111\rangle$ loop, the anisotropy parameter is

$$\alpha_{\frac{1}{2}\langle 111\rangle} = \frac{c_{44}a - (c_{11} + 2c_{12})b}{c_{44}a + 2(c_{11} + 2c_{12})b}. \tag{11}$$

Given the value of α and the total relaxation volume Ω_{rel}, we can reconstruct the dipole tensor for a $\frac{1}{2}[111]$ loop as

$$\begin{aligned} P_{11} = P_{22} = P_{33} = a &= \frac{c_{11} + 2c_{12}}{3}\Omega_{rel}, \\ P_{12} = P_{23} = P_{31} = b &= \frac{c_{44}(\alpha - 1)}{3(1 + 2\alpha)}\Omega_{rel}. \end{aligned} \tag{12}$$

The same process can be followed for a [001] loop, for which the dipole tensor is

$$P_{[001]} = \begin{pmatrix} a & 0 & 0 \\ 0 & a & 0 \\ 0 & 0 & a' \end{pmatrix}. \tag{13}$$

This gives partial relaxation volumes

$$\begin{aligned} \Omega^{(1)} = \Omega^{(2)} &= \frac{c_{11}a}{d} - \frac{c_{12}a'}{d}, \\ \Omega^{(3)} &= -\frac{2c_{12}a}{d} + \frac{(c_{11} + c_{12})a'}{d} \end{aligned} \tag{14}$$

and the anisotropy coefficient

$$\alpha_{\langle 100\rangle} = \frac{c_{11}a - c_{12}a'}{-2c_{12}a + (c_{11} + c_{12})a'}. \tag{15}$$

The parameter d is defined above. Given α and the total relaxation volume Ω_{rel}, we can also reconstruct the dipole tensor for a

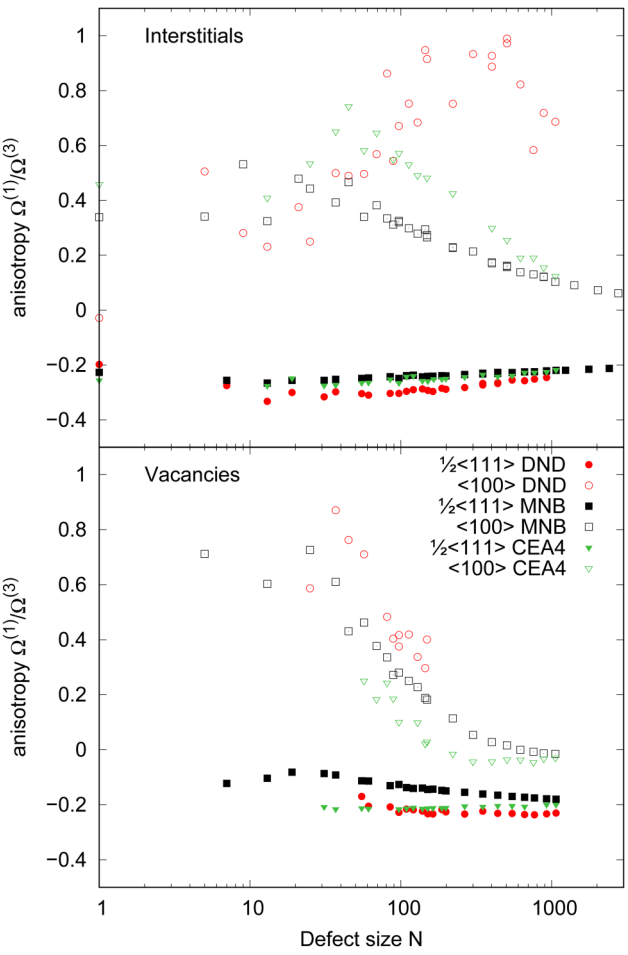

FIG. 7. The relaxation volume anisotropy α, as defined by the ratio of the smallest to the largest partial relaxation volume [see Eq. (10)], for idealized circular prismatic loops.

[001] loop as

$$\begin{aligned} P_{11} = P_{22} = a &= d\frac{c_{12}(\alpha - 1) + c_{11}\alpha}{(c_{11}^2 + c_{11}c_{12} + 2c_{12}^2)(1 + 2\alpha)}\Omega_{rel}, \\ P_{33} = a' &= d\frac{c_{11} + 2c_{12}\alpha}{(c_{11}^2 + c_{11}c_{12} + 2c_{12}^2)(1 + 2\alpha)}\Omega_{rel}, \\ P_{12} = P_{23} = P_{31} &= 0. \end{aligned} \tag{16}$$

For spherical voids, the coefficient $\alpha_{\text{sphere}} = 1$. The dipole tensor for a spherical void can be reconstructed as[20]

$$\begin{aligned} P_{11} = P_{22} = P_{33} &= \frac{c_{11} + 2c_{12}}{3}\Omega_{rel} = K\Omega_{rel}, \\ P_{12} = P_{23} = P_{31} &= 0, \end{aligned} \tag{17}$$

where K is the bulk modulus.

TABLE VIII. The dimensionless relaxation volume anisotropy parameter α, as defined by the ratio of the smallest to the largest partial relaxation volume [see Eq. (10)], for idealized circular prismatic loops, fitted to $\alpha = \alpha_0 + \alpha_1 \ln N/\sqrt{N} + \alpha_2/\sqrt{N} + \alpha_3/N$. The constant term α_0 is derived using linear elasticity [Eqs. (11) and (15)], using the computed values for elastic constants (see Table I).

Method	Structure	α_0	α_1	α_2	α_3
CEA4	v⟨100⟩	0	0.091 ± 0.023	−3.01 ± 0.16	36.8 ± 0.51
MNB	i⟨111⟩	−0.195	−0.144 ± 0.001	0.189 ± 0.006	−0.212 ± 0.018
MNB	i⟨100⟩	0	0.196 ± 0.007	2.320 ± 0.050	−2.47 ± 0.14
MNB	v⟨111⟩	−0.195	0.020 ± 0.003	0.514 ± 0.017	−0.331 ± 0.044
MNB	v⟨100⟩	0	0.567 ± 0.041	−3.16 ± 0.25	19.78 ± 0.66
DND	i⟨111⟩	−0.203	−0.255 ± 0.004	0.270 ± 0.030	−0.216 ± 0.089
DND	i⟨100⟩		5.826 ± 0.075	−19.51 ± 0.47	17.6 ± 1.1
DND	v⟨111⟩	−0.203	−0.226 ± 0.004	0.557 ± 0.029	3.67 ± 0.11
DND	v⟨100⟩	0	−0.254 ± 0.064	5.50 ± 0.36	−0.9 ± 1.3
CEA4	i⟨111⟩	−0.199	−0.128 ± 0.004	0.036 ± 0.028	−0.069 ± 0.081
CEA4	i⟨100⟩	0	0.157 ± 0.033	4.57 ± 0.21	−4.63 ± 0.56
CEA4	v⟨111⟩	−0.199	−0.028 ± 0.002	0.103 ± 0.012	−0.961 ± 0.030

We choose to present a parameterization required to fully reconstruct the dipole tensor as the pair of values $\{\Omega_{rel}, \alpha\}$. The latter is plotted in Fig. 7. Fits to this data are given in Table VIII.

D. Cascade simulations

The final set of configurations we consider are taken from the MD cascade simulations dataset provided for the IAEA Visualization Challenge.[75] The simulations were evolved using a stiffened DND potential[76] until a simulated time 40 ps. The simulation cell was initially a perfect crystal, with damping applied to atoms with kinetic energy over 10 eV[77] and with an additional thermostat at the boundaries of the supercell.[78] One atom was given an initial energy of 50–150 keV, representing a primary knock-on event, and the final temperature was under 1 K. A full description of the methodology is detailed in Refs. 6 and 41. The cascade configurations were relaxed at constant volume using the procedure detailed in Ref. 13 with different EAM potentials, and the relaxation volume was computed using the stress method.

The results for the energy and relaxation volume as a function of the number of Frenkel pairs produced are shown in Fig. 8. We see that there is a slight tendency for a lower energy per Frenkel pair for the largest cascades. This may indicate that the largest cascades (in terms of Frenkel pairs produced) are associated with the largest dislocation loops, and the largest loops have the lowest formation energy per point defect. The relaxation volume shows a clear correlation with the Frenkel pair count, but for individual cascades, there can be considerable variation. This is consistent with the preceding results, if the defect clusters are weakly interacting, as the relaxation volume should be determined by the degree of clustering rather than the total number of defects. On the basis of these simulations, it is reasonable to give a single relaxation volume per cascade. We find from the relaxed cascades

$$\Omega_{rel}/\Omega_0 = b_0 N_{FP}, \tag{18}$$

with $b_0 = 0.77 \pm 0.01$ for MNB and $b_0 = 0.50 \pm 0.02$ for DND.

Finally, we can establish the predictive quality of the tabulated data presented here by using Tables III, V, and VII to estimate the relaxation volume of a cascade configuration. After the initial Wigner-Seitz analysis of the cascade configuration, clusters of interstitials and vacancies were grouped where pairs of like-character point defects were separated by nearest- or next-nearest neighbors. As many clusters are too small to perform a Dislocation eXtraction Algorithm (DXA) analysis,[79] we assume that all the interstitial loops are of $\frac{1}{2}\langle 111\rangle$ type. The relaxation volume for each defect is then looked up, and the total volume summed. The result is displayed in Fig. 9. While there is some scatter for MNB potential, and possibly additional relaxation within the cascade for the DND potential, it is clear that the simple empirical fits for mesoscale defect relaxation volume give a reasonable estimate of the cascade relaxation volume. This is an important result for the transferability of our approach. It indicates that even in the extreme case of high-energy defects formed close together in a cascade, the interaction between defects has a small effect on their relaxation volumes, and so elastically at least the defects can be treated as quasi-independent. This, therefore, demonstrates that the relaxation volume is a "good" phase field for multiscale modeling, in the sense that it is additive with respect to the concentration of defects in the underlying microstructure.

III. DISCUSSION OF RESULTS

A. A comparison with isotropic linear elasticity

In Sec. II C, we defined the anisotropy parameter in the partial relaxation volumes of idealized loop defects considered in Sec. II B. The expected values of the anisotropy parameter can be computed using linear elasticity as follows. The dipole tensor for a dislocation loop with normal $\hat{\mathbf{n}}$, Burgers vector $\mathbf{b}$, and area A in isotropic elasticity is given by[20,80]

$$P_{ij} = A\left[\mu\left(b_i n_j + b_j n_i\right) + \lambda b_k n_k \delta_{ij}\right], \tag{19}$$

where $\mu = (c_{11} - c_{12})/2$ and $\lambda = c_{12}$ are the shear modulus and Lamé constant. Einstein summation over repeated indices is

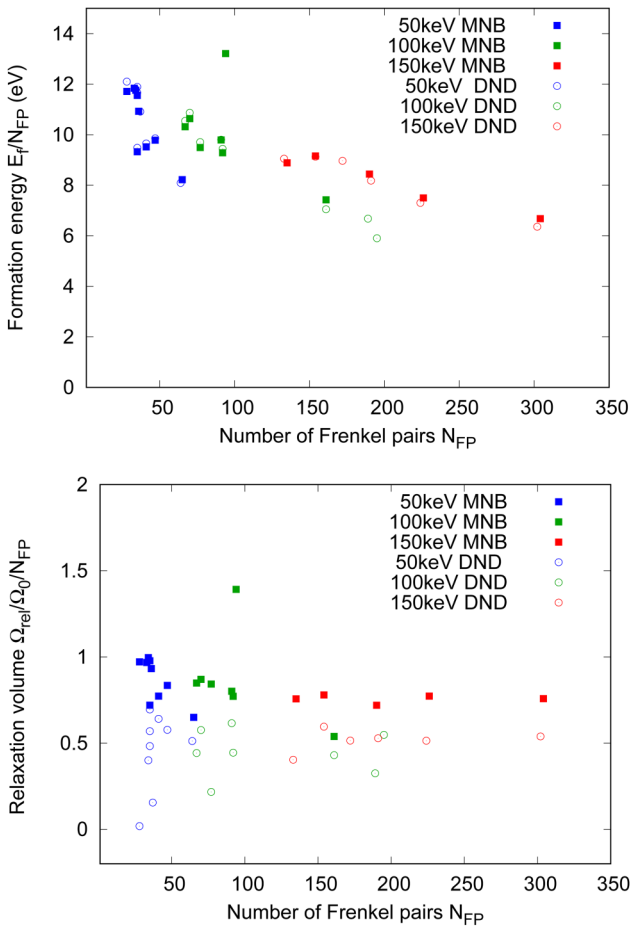

FIG. 8. Formation energy and relaxation volumes of defect clusters generated by MD cascade simulations. Filled symbols: computed with MNB potential; open circles with DND potential. The formation energy of the cascades computed with the two potentials is very similar, but MNB tends to produce a larger relaxation volume. Note that the cascade configurations were generated with the DND potential, then relaxed with both MNB and DND. Note the wide range of number of Frenkel pairs generated in a single cascade, a characteristic of the stochastic process of loop generation,[6] has recently been confirmed experimentally.[43]

assumed. If the normal and Burgers vector are parallel, as is the case here, this expression simplifies to

$$P_{ij} = \pm N\Omega_0\left[2\mu n_i n_j + \lambda\delta_{ij}\right], \tag{20}$$

where the sign is positive for the interstitial loop and negative for a vacancy loop. For the $\frac{1}{2}[111]$ loop, this reduces further to

$$\begin{aligned} P_{11} = P_{22} = P_{33} &= \pm KN\Omega_0, \\ P_{12} = P_{23} = P_{31} &= \pm\frac{2\mu}{3}N\Omega_0, \end{aligned} \tag{21}$$

and so, substituting into Eq. (9), we can identify the relaxation

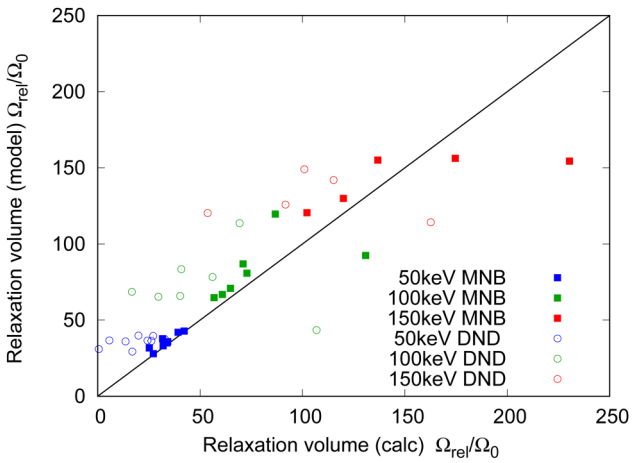

FIG. 9. A comparison of the relaxation volume computed using a full relaxation of the cascade (x-axis) to the relaxation volume predicted using the tabulated fits to the data (Tables III, V, and VII). The diagonal line indicates a 1:1 match—i.e., a perfect reproduction of the relaxation volume.

volume for a $\frac{1}{2}\langle 111\rangle$ loop in isotropic linear elasticity as $\Omega_{rel} = \pm N\Omega_0$ and its anisotropy as $\alpha = (-c_{11} + c_{12} + c_{44})/(2c_{11} - 2c_{12} + c_{44}) = -1/5$. This negative value is significant, as it indicates that for a $\frac{1}{2}\langle 111\rangle$ interstitial loop the lattice expansion is negative in directions orthogonal to the Burgers vector. Values of α computed using computed elastic constants are given in Table VIII. Note that all the potentials give $\alpha \sim -0.2$.

Similarly, for a $\frac{1}{2}[001]$ loop, we find $P_{11} = P_{22} = \pm\lambda N\Omega_0$, $P_{33} = \pm(2\mu + \lambda)N\Omega_0$, and $P_{12} = P_{23} = P_{31} = 0$, and so the relaxation volume computed for a $\langle 100\rangle$ loop in isotropic linear elasticity is also $\Omega_{rel} = \pm N\Omega_0$ but its anisotropy is $\alpha = 0$.

B. Relaxation volume of a vacancy cluster

In this subsection, we derive an analytical formula for the relaxation volume of a mesoscopic spherical vacancy cluster, treating the problem in the linear elasticity approximation. The approach that we adopt here broadly follows the analysis by Wolfer and Ashkin.[81]

The elastic displacement field around a spherical vacancy cluster, taken in the isotropic elasticity approximation, is

$$\mathbf{u}(\mathbf{r}) = \frac{C}{r^2}\mathbf{n} + Dr\mathbf{n}, \tag{22}$$

where C and D are constant factors that we will derive from boundary conditions and $\mathbf{n} = \mathbf{r}/r$. The strain and stress fields associated with the spherical vacancy cluster are[13,81]

$$\begin{aligned} \epsilon_{ij}(\mathbf{r}) &= \frac{C}{r^2}\left(\delta_{ij} - 3n_i n_j\right) + D\delta_{ij}, \\ \sigma_{ij}(\mathbf{r}) &= 2\mu\frac{C}{r^2}\left(\delta_{ij} - 3n_i n_j\right) + 3KD\delta_{ij}, \end{aligned} \tag{23}$$

where, as above, μ is the shear modulus of the material and K is the bulk modulus.

We now find the relaxation volume of a spherical vacancy cluster of radius a embedded in a concentric spherical isotropic elastic medium of radius R. Boundary conditions for surface tractions at the surface of the vacancy cluster ($r = a$) and at the outer surface ($r = R$) have the form

$$\begin{aligned}\sigma_{ij}n_j\big|_{r=a} &= -4\mu\frac{C}{r^3}n_i + 3KDn_i\Big|_{r=a} = -p_a + \frac{2s}{a},\\ \sigma_{ij}n_j\big|_{r=R} &= -4\mu\frac{C}{r^3}n_i + 3KDn_i\Big|_{r=R} = -p_R - \frac{2s}{R},\end{aligned} \tag{24}$$

where p_a is the pressure of gas accumulated inside the vacancy cluster (for example, helium or hydrogen), p_R the external pressure, and s is the orientation-average surface stress. The surface stress s_{ij} is a tensor quantity related to the surface energy by the Shuttleworth relation $s_{ij} = \gamma\delta_{ij} + \partial\gamma/\partial\epsilon_{ij}$, which can be readily computed in atomistic simulation as $s_{ij} = (1/A)\partial(A\gamma)/\partial\epsilon_{ij}$, see Ref. 82. This will have two nonzero eigenvalues which may be computed for each surface orientation. Here, we assume an orientation average, s, will give a good approximation for the total relaxation volume. From the boundary conditions, we find

$$\begin{aligned}C &= \frac{a^3R^3\left(\left(p_a - \frac{2s}{a}\right) - \left(p_R + \frac{2s}{R}\right)\right)}{4\mu(R^3 - a^3)},\\ D &= \frac{a^3\left(p_a - \frac{2s}{a}\right) - R^3\left(p_R + \frac{2s}{R}\right)}{3K(R^3 - a^3)},\end{aligned} \tag{25}$$

which in the limit of zero external pressure ($p_R = 0$), and $R \gg a$ simplify to

$$\begin{aligned}\lim_{p_R=0,R\gg a} C &= \frac{a^3}{4\mu}\left(p_a - \frac{2s}{a}\right),\\ \lim_{p_R=0,R\gg a} D &= 0.\end{aligned}$$

Substituting the coefficients [Eq. (25)] back into Eq. (22) gives the magnitude of the displacement at the outer surface $u(R)$, and hence, the change in volume

$$\Omega_{rel} = \frac{4\pi}{3}(R + u(R))^3 - \frac{4\pi}{3}R^3.$$

After some rearrangement, we find

$$\begin{aligned}\Omega_{rel} = &\frac{-4\pi R^3}{3(3K)^3}\left(p_R + \frac{2s}{R}\right)\\ &\times\left(\left(p_R + \frac{2s}{R}\right)^2 - 9K\left(p_R + \frac{2s}{R}\right) + 27K^2\right)\\ &-\frac{\pi a^3}{\mu(3K)^3}\left(\left(p_R + \frac{2s}{R}\right) - \left(p_a - \frac{2s}{a}\right)\right)\\ &\times\left(p_R + \frac{2s}{R} - 3K\right)^2(3K + 4\mu).\end{aligned} \tag{26}$$

The first term is the response of the outer surface to the external pressure and its surface energy, independent of the presence of the void in the interior. The second term is the relaxation volume due to the void,

$$\begin{aligned}\Omega_{rel} = &-\frac{\pi a^3}{\mu(3K)^3}\left(\left(p_R + \frac{2s}{R}\right) - \left(p_a - \frac{2s}{a}\right)\right)\\ &\times\left(p_R + \frac{2s}{R} - 3K\right)^2(3K + 4\mu).\end{aligned} \tag{27}$$

In the limits $p_R = 0$ and $R \gg a$, this simplifies to an expression for the relaxation volume of a spherical void in an elastic medium, which is filled with gas at pressure p_a,

$$\begin{aligned}\lim_{p_R=0,R\gg a}\Omega_{rel} &= \frac{\pi a^3(p_a - 2s/a)(3K + 4\mu)}{3K\mu}\\ &= \frac{3\pi a^3}{\mu}\left(\frac{1-\nu}{1+\nu}\right)\left(p_a - \frac{2s}{a}\right),\end{aligned} \tag{28}$$

where $\nu = c_{12}/(c_{11} + c_{12}) = \lambda/(2\lambda + 2\mu)$ is Poisson's ratio.

If the internal pressure in the vacancy cluster is zero ($p_a = 0$), or in other words, if there in no helium or hydrogen gas inside the vacancy cluster, the relaxation volume is negative and is proportional to the surface area of the cluster

$$\Omega_{rel} \simeq -6\pi\left(\frac{1-\nu}{1+\nu}\right)\frac{sa^2}{\mu}. \tag{29}$$

The radius of a spherical void can be related to the number of vacancies N it contains

$$N\Omega_0 = \frac{4\pi a^3}{3},$$

where $\Omega_0 = a_0^3/2$ is the volume per atom for a bcc metal, given the lattice constant a_0, so we could also write

$$\Omega_{rel} \simeq -\left(\frac{243\pi}{8}\right)^{1/3}\left(\frac{1-\nu}{1+\nu}\right)\frac{s\,a_0^2}{\mu}N^{2/3}. \tag{30}$$

From this equation, it follows that the relaxation volume "per vacancy" in a vacancy cluster (a void containing no gas) is negative and varies as the average surface stress and as the inverse third power of the number of vacancies contained in the cluster

$$\frac{\Omega_{rel}}{N\Omega_0} \sim -sN^{-1/3}. \tag{31}$$

As a result, the relaxation volume of a void "per vacancy" vanishes in the macroscopic limit $N \gg 1$.

We can compare the relaxation volumes computed using atomistic relaxations to the predictions from the above surface energy model, by substituting the elastic constants and spherically-averaged surface energies γ and stresses s, as computed in the Appendix and tabulated in Table I. If we use a similar surface model for the formation energy, we find the formation

TABLE IX. The leading order constant for the relaxation volumes and formation energies (electronvolts) in the limit of a large spherical void found by fitting to simulation data, as given in Table VII and using a simple model using surface properties only [Eqs. (30) and (32)].

	$\Omega_{rel}/\Omega_0/N^{2/3}$		$E_f/N^{2/3}$	
	Fit to simulation data	Surface stress model	Fit to simulation data	Surface energy model
DFT	−0.49	−0.66	7.18	7.08
MNB	−0.50	−0.41	7.35	7.14
DND	−0.31	−0.20	5.25	5.31
CEA4	−0.12	−0.16	5.56	5.33

energy per vacancy varies as the average surface energy and the inverse third power of the number of vacancies that it contains

$$\begin{aligned} E_f &\simeq 4\pi\gamma a^2 \\ &\simeq (9\pi)^{1/3}\,\gamma a_0^2\,N^{2/3}, \\ E_f/N &\sim \gamma\,N^{-1/3}. \end{aligned} \tag{32}$$

The comparison is shown in Table IX. We conclude that the relaxation volume and formation energy of voids in tungsten are well reproduced by a simple surface model.

C. A comparison of the empirical potentials used

It is instructive to consider why two potentials which give very similar energies of formation for lattice defects nevertheless give quite different elastic properties. As shown in Eq. (5), the dipole tensor depends on the first derivative of the potential, and for the pairwise part $V(r_{ab})$ at least this is straightforward to analyze. The MNB potential descends from the smooth Ackland-Thetford form,[47,48] whereas the DND potential is based on a piecewise cubic-spline form. This latter form has a continuous second derivative, but discontinuous third, leading to cusps in the second derivative. In the case of the DND potential, this second derivative swings from large positive to negative values. This, in turn, means that small changes in relative atom positions lead to large changes in the forces on the atoms. The MNB potential, by contrast, has a fairly flat first derivative. The CEA-4 potential,[44] which is also a cubic-spline form, but included fitting to forces during its construction, shares this flat first derivative for near equilibrium atom separations, but with more structure for greatly distorted structures. This is illustrated in Fig. 10.

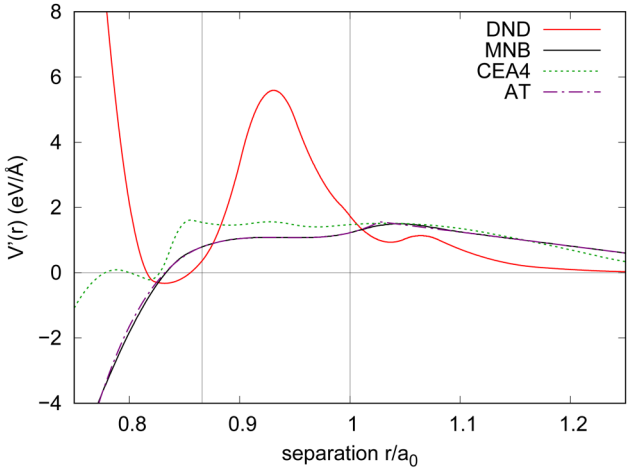

FIG. 10. The first derivative of the pairwise part of selected empirical potentials, in the effective gauge[47,83] where $\rho_{eq} = 1$, $F[0] = F[1] = 0$. The MNB potential is descended from the smooth Ackland-Thetford form,[47,48] whereas the DND potential is a piecewise cubic-spline which did not consider the first derivative during fitting. Vertical lines are drawn at first and second nearest neighbor positions. Note that the DND potential is not unstable at short separation, as might be inferred from this plot, as it is stabilized by its many-body part. In MD simulations, the Ziegler-Biersack-Littmark (ZBL) correction is also generally applied at short range.[76,84] The Ackland-Thetford pairwise potential is very similar to the MNB.

D. Estimating the relaxation volume per collision cascade

In Sec. II D, we found that the relaxation volume per cascade is proportional to the number of Frenkel pairs contained. We can make an estimate for the relaxation volume per cascade if we make the assumption that the lattice defects are isolated and idealized. Sand *et al.*[6] suggest that clusters should be produced in cascades with a frequency given by the power-law

$$f(N) = A/N^s, \tag{33}$$

and Ref. 85 gives exponents for large clusters for interstitial-type and vacancy clusters in bulk tungsten cascade simulations as $s_I = 1.6$ and $s_V = 2.0$, respectively. The expected relaxation volume per Frenkel pair is then,

$$\Omega_{rel}/N_{FP} = \sum_{N=1}^{N_{\max}} q_I(N)\Omega_I(N) + q_V(N)\Omega_V(N), \tag{34}$$

with $q_{I/V}(N)$ being the weighting for an interstitial/vacancy cluster containing N point defects,

$$q_I(N) = \frac{N^{-S_I}}{\sum_{N=1}^{N_{\max}} N^{1-S_I}}, \quad q_V(N) = \frac{N^{-S_V}}{\sum_{N=1}^{N_{\max}} N^{1-S_V}}. \tag{35}$$

Note that $\sum_{N=1}^{N_{\max}} N q_I(N) = \sum_{N=1}^{N_{\max}} N q_V(N) = 1$. We use a limit, $N_{\max}$, for the number of point defects in a single defect, as an infinite sized defect cannot be produced in a single subcascade.[41,86]

As a first order approximation, we can write the relaxation volumes of interstitial/vacancy clusters using their leading terms, $\Omega_I(N)/\Omega_0 \sim N + b_0^{(I)}\sqrt{N}\log N + b_1^{(I)}\sqrt{N}$ and $\Omega_V(N)/\Omega_0 \sim b_0^{(V)}N^{2/3}$. Then, we can write down the relaxation volume per

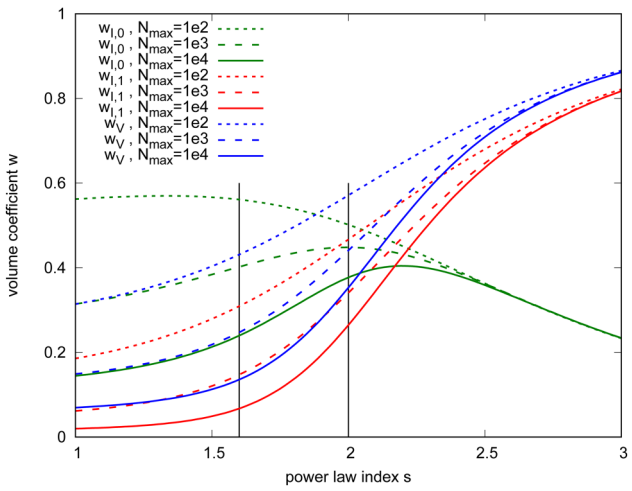

FIG. 11. Relaxation volume coefficients for cascades characterized by power-laws for the size-frequency distributions of interstitial loops and vacancy clusters, with power-law indices s_I and s_V. The relaxation volumes per point defect for a cascade can be written as $\Omega_{rel}/\Omega_0/N_{FP} = 1 + b_0^{(I)} w_{I,0} + b_1^{(I)} w_{I,1} + b_0^{(V)} w_V$. Vertical lines indicate the power indices measured using MD for 150 keV PKA cascades in tungsten.[85]

Frenkel pair for the cascade as

$$\Omega_{rel}/\Omega_0/N_{FP} = 1 + b_0^{(I)} w_{I,0} + b_1^{(I)} w_{I,1} + b_0^{(V)} w_V, \tag{36}$$

where

$$w_{I,0} = \frac{\sum_{N=1}^{N_{\max}} ln(N) N^{1/2-s_I}}{\sum_{N=1}^{N_{\max}} N^{1-s_I}},$$
$$w_{I,1} = \frac{\sum_{N=1}^{N_{\max}} N^{1/2-s_I}}{\sum_{N=1}^{N_{\max}} N^{1-s_I}},$$
$$w_V = \frac{\sum_{N=1}^{N_{\max}} N^{2/3-s_V}}{\sum_{N=1}^{N_{\max}} N^{1-s_V}}.$$

The coefficients $w_{I,0}$, $w_{I,1}$, w_V, which determine the relative importance of interstitial and vacancy contributions to the relaxation volume, are plotted in Fig. 11. For the tungsten cascades, we consider $N_{\max} \sim 1000$, $s_I = 1.6$, and $s_V = 2.0$, and so $w_{I,0} \simeq 0.40$, $w_{I,1} \simeq 0.15$, and $w_V \simeq 0.44$. We find in this work $b_0^{(I)} = 0.008$, $b_1^{(I)} = 0.738$, and $b_0^{(V)} = -0.50$ for the MNB potential (see Tables V and VII), and so expect $\Omega_{rel}/\Omega_0/N_{FP} \sim 0.89$.

We could get a slightly better estimate for the total cascade relaxation volume by using the $\Omega_{I/V}(N)$ given by the values for the smallest clusters in Table III, the full expressions given by the fits in Table VII, and Table V for larger clusters. This gives the values $\Omega_{rel}/\Omega_0/N_{FP} = 0.87$ for MNB. For DND and CEA4, the prefactor is 0.80 and 1.31, respectively. Though not a perfect match to the observed total relaxation volumes computed in Sec. II D, this simple calculation returns that MNB has a larger relaxation volume than DND and that both have a scaling factor a little under unity.

IV. IMPLICATIONS FOR MODELING MICROSTRUCTURAL EVOLUTION UNDER IRRADIATION

We noted earlier that, in agreement with the analysis performed in Refs. 26 and 27, the fact that the relaxation volume of a self-interstitial atom defect is positive and fairly large, whereas the relaxation volume of a vacancy is negative and relatively small, represents the fundamental reason why metals expand and swell under irradiation. The dynamics of accumulation of defects, involving their recombination and coalescence, gives rise to a fairly complex picture of microstructural evolution, where internal stresses and strains as well as the volume of a reactor component exposed to irradiation vary as functions of time. For example, some volumetric expansion occurs effectively instantaneously as a result of the generation of defects in collision cascades,[87–90] see Fig. 1, due to the fact that the total (positive) relaxation volume of all the self-interstitial defects produced in a cascade is greater than the (negative) relaxation volume of all the vacancies. This is confirmed by the analysis given in Sec. III D above, which also shows that no notion of diffusion-mediated microstructural evolution is required to arrive at the conclusion that the production of defects in cascades gives rise to swelling.

Using the equations for relaxation volumes of defect clusters given above, it is possible to evaluate the degree of volumetric expansion of a material even in the limit where the voids formed under irradiation are too small to be visible in an electron microscope. Also, the formulas for defect relaxation volumes are directly applicable for computing the volumetric expansion of an evolving microstructure simulated using object kinetic Monte Carlo.[9,91,92]

In the mesoscopic limit, the relaxation volumes of dislocation loops, of either self-interstitial and vacancy nature, can be evaluated as line integrals over the loop perimeters,[20,93]

$$\Omega_{rel} = -\frac{1}{2}\oint_\Gamma \mathbf{b}\cdot(\mathbf{r}\times d\mathbf{l}),$$
$$\frac{d\Omega_{rel}}{dt} = -\oint_\Gamma \mathbf{b}\cdot(\mathbf{v}\times d\mathbf{l}), \tag{37}$$

where $\mathbf{r}$ and $\mathbf{v}$ are the position and velocity of a point on a dislocation line, and the choice of the sign before the integral depends on the Burgers vector convention.[20] Equation (37), together with the formula for the relaxation volume of a void or a gas bubble (28), enables evaluating volumetric swelling in the limit where radiation defect objects are mesoscopic or even macroscopic. In this limit, the degree of volumetric swelling may be assessed by analyzing the relaxation volume of dislocation loops, which are often readily seen in electron microscope images, rather than the void component of microstructure.

The treatment of the dynamics of diffusion-mediated evolution of microstructure is beyond the scope of this paper, although it would be appropriate to note that Eq. (37) for the rate of variation of relaxation volume of dislocations provides a link between diffusion-mediated models for microstructural evolution[81,94–96] and

the stress and strain based treatment of radiation-induced volumetric swelling of a material given above in this paper.

V. CONCLUSIONS

In this paper, we have computed the relaxation volumes of a broad variety of lattice defects in tungsten, using three empirical potentials and density functional theory. We have presented the data in a number of scatter plots but have also presented tabulated data for empirical fits to the results. It is hoped that the data in this form is readily applicable to a range of coarse-grained models, which involve either the elastic interactions between defects or the stresses and strains induced by the defect population.

We have found that there is some considerable variation in the absolute values of relaxation volumes of defects compared across the EAM potentials we have considered. This is because the elastic properties of defects were never considered in the parameter fitting. We were, however, able to identify some cross-potential trends. The relaxation volume per point defect varies according the specific configuration of the defect cluster, but for small defect clusters ($N < 10$) is likely to remain in the range $\pm 10\%$. This means that knowing the point defect content of a cluster and its character (vacancy- or interstitial-type) is sufficient to predict the relaxation volume of a cluster. Larger defect clusters ($N > 10$) are most stable as dislocation loops, categorized by a Burgers vector, or in the case of vacancies are more stable as voids ($N < 6 \times 10^5$ for MNB or $N < 3 \times 10^6$ for CEA4,[72] and we find $N < 8 \times 10^6$ for DND). $\frac{1}{2}\langle 111\rangle$ and $\langle 100\rangle$ dislocation loops and voids are sufficiently dissimilar to require their own representation of relaxation volume as a function of defect size, to predict their elastic properties.

We showed in Sec. II D that the relaxation volume of a cascade is proportional to the number of Frenkel pairs it contains, with a positive coefficient around unity. The structure in the relaxation volume per point defect is to some extent averaged out by the range of sizes of defects produced in a cascade. The expected number of Frenkel pairs per cascade is itself proportional to the PKA energy, according to the Norgett-Robinson-Torrens (NRT) formula,[97] a result broadly confirmed by the MD simulation,[4,98] though the constant of proportionality is now widely held to be somewhat smaller than that given by the NRT model. The recent arc-dpa model[99,100] predicts the number of Frenkel pairs per cascades produced in a defect-free material at low energy to be slightly above the line of proportionality seen at high energy, but we can still say that as a rule-of-thumb, the relaxation volume per cascade increases roughly linearly with the PKA energy. As the defect microstructure evolves, annihilation between vacancy-type and interstitial-type will reduce the total relaxation volume. This is a much more significant effect than deviations in proportionality of the total volume of initial defects to the PKA energy, but it will nevertheless preserve approximately the linear dependence of relaxation volume with Frenkel pair count. Coalescence of small defect clusters will have a smaller effect on the linear dependence of the relaxation volume with Frenkel pair count. As we have found a potential-dependent nonmonotonic variation of the relaxation volume of individual dislocation loops with point defect count N, it is not clear at this point whether coalescence will increase or decrease the relaxation volume. DFT calculations of the dipole tensors of large loops may be able to answer this question in the future.

ACKNOWLEDGMENTS

This work has been carried out within the framework of the EUROfusion Consortium and has received funding from Euratom Research and Training Programme 2019-2020 under Grant Agreement No. 633053 and from the RCUK Energy Programme (Grant No. EP/P012450/1). The views and opinions expressed herein do not necessarily reflect those of the European Commission. D.N.M. acknowledges the support from high-performance computing facility MARCONI (Italy) through the EUROfusion HPC project AMPSTANI (2017-2019). A.E.S. acknowledges support from the Academy of Finland through Project No. 311472.

APPENDIX: AVERAGE SURFACE ENERGY

In this appendix, we find the average surface energy suitable for a spherical void, given calculated values of the surface energy on facets. As we are working with cubic crystals, we expand the surface energy in cubic harmonics

$$Y_{mn}(x, y, z) = \left(x^4 + y^4 + z^4\right)^m \left(x^2 y^2 z^2\right)^n, \tag{A1}$$

where x, y, z are direction cosines so that the surface energy at a general direction is interpolated as

$$g(x, y, z) = \sum_{mn} a_{mn} Y_{mn}(x, y, z). \tag{A2}$$

We can fit available surface data to the lowest orders of Y_{mn}. It is most common in the literature to see data for $\langle 110\rangle$, $\langle 100\rangle$, $\langle 211\rangle$, and $\langle 111\rangle$ planes, in which case it suffices to take $0 \le m, n \le 1$. Writing the surface energy for the $\langle 110\rangle$ plane as $\gamma_{\langle 110\rangle}$, and similarly for the others, we find

$$\begin{aligned} a_{00} &= -\gamma_{\langle 100\rangle} + 2\gamma_{\langle 110\rangle}, \\ a_{10} &= 2(\gamma_{\langle 100\rangle} - \gamma_{\langle 110\rangle}), \\ a_{01} &= 27(\gamma_{\langle 100\rangle} + 3\gamma_{\langle 111\rangle} - 4\gamma_{\langle 211\rangle}), \\ a_{11} &= -54(\gamma_{\langle 100\rangle} + 3\gamma_{\langle 111\rangle} - 6\gamma_{\langle 211\rangle} + 2\gamma_{\langle 110\rangle}). \end{aligned} \tag{A3}$$

The spherically-averaged surface energy, γ, can be found by integrating over the surface of the sphere

$$\begin{aligned} \gamma &= \frac{1}{4\pi} \int_{\theta=0}^{\pi} \int_{\phi=0}^{2\pi} g(\sin\theta\cos\phi,\ \sin\theta\sin\phi,\ \cos\theta) \sin\theta \, d\theta \, d\phi \\ &= a_{00} + \frac{a_{01}}{105} + \frac{3a_{10}}{5} + \frac{a_{11}}{231} \\ &= \frac{1}{385}\left(86\gamma_{\langle 100\rangle} + 128\gamma_{\langle 110\rangle} + 27\gamma_{\langle 111\rangle} + 144\gamma_{\langle 211\rangle}\right). \end{aligned} \tag{A4}$$

It should be noted that two assumptions are made here, firstly, that voids are unfaceted, and secondly, that the surface energy

varies smoothly with the orientation of the facet, so this interpolation should not be applied uncritically to other cases. However, this simple expression does give a single value for surface energy suitable for use in our analytical calculations of void relaxation volumes.

REFERENCES

[1]J. Marian, C. S. Becquart, C. Domain, S. L. Dudarev, M. R. Gilbert, R. J. Kurtz, D. R. Mason, K. Nordlund, A. E. Sand, L. L. Snead, T. Suzudo, and B. D. Wirth, "Recent advances in computational materials modeling of tungsten as plasma-facing material for fusion energy applications," Nucl. Fusion **57**(9), 092008 (2017).

[2]D. Nguyen-Manh, M. Y. Lavrentiev, M. Muzyk, and S. L. Dudarev, "First-principles models for phase stability and radiation defects in structural materials for future fusion power-plant applications," J. Mater. Sci. **47**, 7385–7398 (2012).

[3]S. L. Dudarev, "Density functional theory models for radiation damage," Annu. Rev. Mater. Res. **43**, 35–61 (2013).

[4]A. F. Calder and D. J. Bacon, "A molecular dynamics study of displacement cascades in α-iron," J. Nucl. Mater. **207**, 25–45 (1993).

[5]R. E. Stoller and L. R. Greenwood, "Subcascade formation in displacement cascade simulations: Implications for fusion reactor materials," J. Nucl. Mater. **271–272**, 57–62 (1999).

[6]A. E. Sand, S. L. Dudarev, and K. Nordlund, "High-energy collision cascades in tungsten: Dislocation loops structure and clustering scaling laws," Europhys. Lett. **103**(4), 46003 (2013).

[7]L. K. Béland, P. Brommer, F. El-Mellouhi, J.-F. Joly, and N. Mousseau, "Kinetic activation-relaxation technique," Phys. Rev. E **84**, 046704 (2011).

[8]H. Xu, Y. N. Osetsky, and R. E. Stoller, "Self-evolving atomistic kinetic Monte-Carlo: Fundamentals and applications," J. Phys. Condens. Matter **24**(37), 375402 (2012).

[9]D. R. Mason, X. Yi, M. A. Kirk, and S. L. Dudarev, "Elastic trapping of dislocation loops in cascades in ion-irradiated tungsten foils," J. Phys. Condens. Matter **26**(37), 375701 (2014).

[10]J. Marian and V. V. Bulatov, "Stochastic cluster dynamics method for simulations of multispecies irradiation damage accumulation," J. Nucl. Mater. **415**(1), 84–95 (2011).

[11]A. Y. Dunn, L. Capolungo, E. Martinez, and M. Cherkaoui, "Spatially resolved stochastic cluster dynamics for radiation damage evolution in nanostructured metals," J. Nucl. Mater. **443**(1), 128–139 (2013).

[12]X. Yi, A. E. Sand, D. R. Mason, M. A. Kirk, S. G. Roberts, K. Nordlund, and S. L. Dudarev, "Direct observation of size scaling and elastic interaction between nano-scale defects in collision cascades," Europhys. Lett. **110**(3), 36001 (2015).

[13]S. L. Dudarev, D. R. Mason, E. Tarleton, P.-W. Ma, and A. E. Sand, "Multi-scale model for stresses, strains and swelling of reactor components under irradiation," Nucl. Fusion **58**, 126002 (2018).

[14]F. Hofmann, X. Song, T.-S. Jun, B. Abbey, M. Peel, J. Daniels, V. Honkimäki, and A. M. Korsunsky, "High energy transmission micro-beam Laue synchrotron X-ray diffraction," Mater. Lett. **64**(11), 1302–1305 (2010).

[15]F. Hofmann, D. Nguyen-Manh, M. R. Gilbert, C. E. Beck, J. K. Eliason, A. A. Maznev, W. Liu, D. E. J. Armstrong, K. A. Nelson, and S. L. Dudarev, "Lattice swelling and modulus change in a helium-implanted tungsten alloy: X-ray micro-diffraction, surface acoustic wave measurements, and multiscale modelling," Acta Mater. **89**, 352–363 (2015).

[16]W. Hertz, W. Waidelich, and H. Peisl, "Lattice contraction due to quenching in vacancies in platinum and gold," Phys. Lett. A **43**(3), 289–290 (1973).

[17]S. J. Zinkle and N. M. Ghoniem, "Operating temperature windows for fusion reactor structural materials," Fusion Eng. Des. **51–52**, 55–71 (2000).

[18]H. Bolt, V. Barabash, G. Federici, J. Linke, A. Loarte, J. Roth, and K. Sato, "Plasma facing and high heat flux materials—Needs for ITER and beyond," J. Nucl. Mater. **307–311**(Pt. 1), 43–52 (2002).

[19]S. J. Zinkle and G. S. Was, "Materials challenges in nuclear energy," Acta Mater. **61**(3), 735–758 (2013).

[20]S. L. Dudarev and P.-W. Ma, "Elastic fields, dipole tensors, and interaction between self-interstitial atom defects in bcc transition metals," Phys. Rev. Mater. **2**, 033602 (2018).

[21]P.-W Ma and S. L. Dudarev, "Universality of point defect structure in body-centred cubic metals," Phys. Rev. Mater. **3**, 013605 (2019).

[22]P.-W. Ma and S. L. Dudarev, "Symmetry-broken self-interstitial defects in chromium, molybdenum, and tungsten," Phys. Rev. Mater. **3**, 043606 (2019).

[23]W. Schilling, "Self-interstitial atoms in metals," J. Nucl. Mater. **69–70**, 465–489 (1978).

[24]W. G. Wolfer, "A novel approach to compute the relaxation volume of self-interstitials in metals," J. Phys. Metal Phys. **12**, 425–433 (1982).

[25]Y. Kraftmakher, "Equilibrium vacancies and thermophysical properties of metals," Phys. Rep. **299**, 79–188 (1998).

[26]W. G. Wolfer, "The dislocation bias," J. Comput. Aided Mater. Des. **14**, 403–417 (2007).

[27]M. P. Surh, J. B. Sturgeon, and W. G. Wolfer, "Void nucleation, growth, and coalescence in irradiated metals," J. Nucl. Mater. **378**, 86–97 (2008).

[28]R. Benedek, L. H. Yang, C. Woodward, and B. I. Min, "Formation energy and lattice relaxation for point defects in Li and Al," Phys. Rev. B **45**, 2607–2612 (1992).

[29]R. Pawellek, M. Fahnle, C. Elsasser, K. M. Ho, and C. T. Chan, "First-principles calculation of the relaxation around a vacancy and the vacancy formation energy in BCC Li," J. Phys. Condens. Matter **3**(14), 2451–2455 (1991).

[30]W. Frank, U. Breier, C. Elsässer, and M. Fähnle, "Properties of monovacancies and self-interstitials in bcc Li: An *ab initio* pseudopotential study," Phys. Rev. B **48**, 7676–7678 (1993).

[31]W. Frank, U. Breier, C. Elsässer, and M. Fähnle, "First-principles calculations of absolute concentrations and self-diffusion constants of vacancies in lithium," Phys. Rev. Lett. **77**, 518–521 (1996).

[32]U. Breier, W. Frank, C. Elsässer, M. Fähnle, and A. Seeger, "Properties of monovacancies and self-interstitials in bcc Na: An ab initio pseudopotential study," Phys. Rev. B **50**, 5928–5936 (1994).

[33]V. Schott, M. Fähnle, and P. A. Madden, "Theory of self-diffusion in alkali metals: I. Results for monovacancies in Li, Na, and K," J. Phys. Condens. Matter **12**(7), 1171–1194 (2000).

[34]M. Rieth, J. L. Boutard, S. L. Dudarev, T. Ahlgren, S. Antusch, N. Baluc, M.-F. Barthe, C. S. Becquart, L. Ciupinski, J. B. Correia, C. Domain, J. Fikar, E. Fortuna, C.-C. Fu, E. Gaganidze, T. L. Galán, C. García-Rosales, B. Gludovatz, H. Greuner, K. Heinola, N. Holstein, N. Juslin, F. Koch, W. Krauss, K. J. Kurzydlowski, J. Linke, Ch. Linsmeier, N. Luzginova, H. Maier, M. S. Martínez, J. M. Missiaen, M. Muhammed, A. Muñoz, M. Muzyk, K. Nordlund, D. Nguyen-Manh, P. Norajitra, J. Opschoor, G. Pintsuk, R. Pippan, G. Ritz, L. Romaner, D. Rupp, R. Schäublin, J. Schlosser, I. Uytdenhouwen, J. G. van der Laan, L. Veleva, L. Ventelon, S. Wahlberg, F. Willaime, S. Wurster, and M. A. Yar, "Review on the EFDA programme on tungsten materials technology and science," J. Nucl. Mater. **417**(1–3), 463–467 (2011).

[35]M. Rieth, S. L. Dudarev, S. M. Gonzalez de Vicente *et al.*, "Recent progress in research on tungsten materials for nuclear fusion applications in Europe," J. Nucl. Mater. **432**(1–3), 482–500 (2013).

[36]F. H Featherston and J. R. Neighbours, "Elastic constants of tantalum, tungsten, and molybdenum," Phys. Rev. **130**, 1324–1333 (1963).

[37]A. Stukowski, "Visualization and analysis of atomistic simulation data with OVITO—The open visualization tool," Model. Simul. Mater. Sci. Eng. **18**, 015012 (2010).

[38]R. A. Johnson, "Point-defect calculations for tungsten," Phys. Rev. B **27**, 2014–2018 (1983).

[39]D. Kato, H. Iwakiri, and K. Morishita, "Formation of vacancy clusters in tungsten crystals under hydrogen-rich condition," J. Nucl. Mater. **417**(1), 1115–1118 (2011).

[40]P. M. Derlet, D. Nguyen-Manh, and S. L. Dudarev, "Multiscale modeling of crowdion and vacancy defects in body-centered-cubic transition metals," Phys. Rev. B **76**, 054107 (2007).
[41]A. E. Sand, D. R. Mason, A. De Backer, X. Yi, S. L. Dudarev, and K. Nordlund, "Cascade fragmentation: Deviation from power law in primary radiation damage," Mater. Res. Lett. **5**(5), 357–363 (2017).
[42]D. R. Mason, A. E. Sand, X. Yi, and S. L. Dudarev, "Direct observation of the spatial distribution of primary cascade damage in tungsten," Acta Mater. **144**, 905–917 (2018).
[43]D. R. Mason, X. Yi, A. E. Sand, and S. L. Dudarev, "Experimental observation of the number of visible defects produced in individual primary damage cascades in irradiated tungsten," Europhys. Lett. **122**(6), 66001 (2018).
[44]M.-C. Marinica, L. Ventelon, M. R. Gilbert, L. Proville, S. L. Dudarev, J. Marian, G. Bencteux, and F. Willaime, "Interatomic potentials for modelling radiation defects and dislocations in tungsten," J. Phys. Condens. Matter **25**(39), 395502 (2013).
[45]G. J. Ackland, M. I. Mendelev, D. J. Srolovitz, S. Han, and A. V. Barashev, "Development of an interatomic potential for phosphorus impurities in α-iron," J. Phys. Condens. Matter **16**(27), S2629 (2004).
[46]D. R. Mason, D. Nguyen-Manh, and C. S. Becquart, "An empirical potential for simulating vacancy clusters in tungsten," J. Phys. Condens. Matter **29**(50), 505501 (2017).
[47]M. W. Finnis and J. E. Sinclair, "A simple empirical n-body potential for transition metals," Philos. Mag. A **50**(1), 45–55 (1984).
[48]G. J. Ackland and R. Thetford, "An improved n-body semi-empirical model for body-centred cubic transition metals," Philos. Mag. A **56**, 15–30 (1987).
[49]A. M. Kossevich, *The Crystal Lattice* (Wiley-VCH, Berlin, 1999).
[50]C. B. Barber, D. P. Dobkin, and H. T. Huhdanpaa, "The quickhull algorithm for convex hulls," ACM Trans. Math. Softw. **22**(4), 469–483 (1996).
[51]Note that this same excess linear correction r would be required to find the volume of a periodic supercell from the convex hull of the atoms contained within.
[52]H. Kanzaki, "Point defects in face-centred cubic lattice-l distortion around defects," J. Phys. Chem. Solids **2**, 24–36 (1957).
[53]C. Domain and C. S. Becquart, "Ab initio calculations of defects in Fe and dilute Fe-Cu alloys," Phys. Rev. B **65**, 024103 (2001).
[54]D. M. Barnett, "The precise evaluation of derivatives of the anisotropic elastic Green's functions," Phys. Status Solidi B **49**, 741–748 (1972).
[55]C. Varvenne and E. Clouet, "Elastic dipoles of point defects from atomistic simulations," Phys. Rev. B **96**, 224103 (2017).
[56]G. Leibfried and N. Breuer, *Point Defects in Metals* (Springer, Berlin, 1978).
[57]C. Varvenne, F. Bruneval, M.-C. Marinica, and E. Clouet, "Point defect modeling in materials: Coupling *ab initio* and elasticity approaches," Phys. Rev. B **88**, 134102 (2013).
[58]F. H. Featherstone and J. R. Neighbours, "Elastic constants of tantalum, tungsten, and molybdenum," Phys. Rev. **130**, 1324–1333 (1963).
[59]F. R. de Boer, R. Boom, W. C. M. Mattens, A. R. Miedema, and A. K. Niessen, *Cohesion in Metals* (North-Holland, Amsterdam, 1988).
[60]G. Kresse and J. Hafner, "Ab initio molecular dynamics for liquid metals," Phys. Rev. B **47**, 558–561 (1993).
[61]G. Kresse and J. Furthmüller, "Efficient iterative schemes for ab initio total-energy calculations using a plane-wave basis set," Phys. Rev. B **54**, 11169–11186 (1996).
[62]G. Kresse and J. Furthmüller, "Efficiency of ab-initio total energy calculations for metals and semiconductors using a plane-wave basis set," Comput. Mater. Sci. **6**(1), 15–50 (1996).
[63]D. Nguyen-Manh, A. P. Horsfield, and S. L. Dudarev, "Self-interstitial atom defects in bcc transition metals: Group-specific trends," Phys. Rev. B **73**, 020101 (2006).
[64]D. Nguyen-Manh and S. L. Dudarev, "Trapping of He clusters by inert-gas impurities in tungsten: First-principles predictions and experimental validation," Nucl. Instrum. Methods Phys. Res. B **352**, 86–91 (2015).
[65]A. E. Sand, J. Dequeker, C. S. Becquart, C. Domain, and K. Nordlund, "Non-equilibrium properties of interatomic potentials in cascade simulations in tungsten," J. Nucl. Mater. **470**(Suppl. C), 119–127 (2016).
[66]J. P. Perdew, K. Burke, and M. Ernzerhof, "Generalized gradient approximation made simple," Phys. Rev. Lett. **77**, 3865–3868 (1996).
[67]R. Alexander, M.-C. Marinica, L. Proville, F. Willaime, K. Arakawa, M. R. Gilbert, and S. L. Dudarev, "*Ab initio* scaling laws for the formation energy of nanosized interstitial defect clusters in iron, tungsten, and vanadium," Phys. Rev. B **94**, 024103 (2016).
[68]M.-C. Marinica, F. Willaime, and J.-P. Crocombette, "Irradiation-induced formation of nanocrystallites with C15 Laves phase structure in bcc iron," Phys. Rev. Lett **108**, 025501 (2012).
[69]N. Gao, W. Setyawan, R. J. Kurtz, and Z. Wang, "Effects of applied strain on nanoscale self-interstitial cluster formation in bcc iron," J. Nucl. Mater. **493**, 62–68 (2017).
[70]X. Yi, M. L. Jenkins, M. Briceno, S. G. Roberts, Z. Zhou, and M. A. Kirk, "In situ study of self-ion irradiation damage in W and W-5Re at 500 °C," Philos. Mag. **93**(14), 1715–1738 (2013).
[71]J. Fikar and R. Gröger, "Shape of small prismatic dislocation loops in tungsten and iron," in *Materials Structure & Micromechanics of Fracture VIII*, Solid State Phenomena Vol. 258 (Trans Tech Publications, 2017), pp. 97–101.
[72]J. Fikar, R. Schäublin, D. R. Mason, and D. Nguyen-Manh, "Nano-sized prismatic vacancy dislocation loops and vacancy clusters in tungsten," Nucl. Mater. Energy **16**, 60–65 (2018).
[73]M. R. Gilbert, S. L. Dudarev, P. M. Derlet, and D. G. Pettifor, "Structure and metastability of mesoscopic vacancy and interstitial loop defects in iron and tungsten," J. Phys. Condens. Matter **20**(34), 345214 (2008).
[74]P. Diaconis and B. Efron, "Computer-intensive methods in statistics," Sci. Am. **248**, 116–130 (1983).
[75]See https://challenge.iaea.org/challenges/2018-NA-Mat-Fusion/about for "The Quest for Clean Energy: IAEA Challenge on Materials for Fusion" (last accessed April 2018).
[76]C. Björkas, K. Nordlund, and S. L. Dudarev, "Modelling radiation effects using the ab-initio based tungsten and vanadium potentials," Nucl. Instrum. Methods Phys. Res. Phys. Res. B **267**, 3204–3208 (2009).
[77]A. E. Sand and K. Nordlund, "On the lower energy limit of electronic stopping in simulated collision cascades in Ni, Pd and Pt," J. Nucl. Mater. **456**, 99–105 (2015).
[78]H. J. C. Berendsen, J. P. M. Postma, W. F. van Gunsteren, A. DiNola, and J. R. Haak, "Molecular dynamics with coupling to an external bath," J. Chem. Phys. **81**, 3684 (1998).
[79]A. Stukowski, V. V. Bulatov, and A. Arsenlis, "Automated identification and indexing of dislocations in crystal interfaces," Model. Simul. Mater. Sci. Eng. **20**, 085007 (2012).
[80]S. L. Dudarev and A. P. Sutton, "Elastic interactions between nano-scale defects in irradiated materials," Acta Mater. **125**, 425–430 (2017).
[81]W. G. Wolfer and M. Ashkin, "Stress-induced diffusion of point defects to spherical sinks," J. Appl. Phys. **46**(2), 547–557 (1975).
[82]T. Frolov and Y. Mishin, "Temperature dependence of the surface free energy and surface stress: An atomistic calculation for Cu(110)," Phys. Rev. B **79**, 045430 (2009).
[83]G. Bonny, P. Grigorev, and D. Terentyev, "On the binding of nanometric hydrogen-helium clusters in tungsten," J. Phys. Condens. Matter **26**(48), 485001 (2014).
[84]J. F. Ziegler, J. P. Biersack, and U. Littmark, *The Stopping and Range of Ions in Solids* (Pergamon, 1982).
[85]A. E. Sand, M. J. Aliaga, M. J. Caturla, and K. Nordlund, "Surface effects and statistical laws of defects in primary radiation damage: Tungsten vs. iron," Europhys. Lett. **115**(3), 36001 (2016).
[86]A. De Backer, A. E. Sand, K. Nordlund, L. Luneville, D. Simeone, and S. Dudarev, "Subcascade formation and defect cluster size scaling in high-energy collision events in metals," Europhys. Lett. **115**(2), 26001 (2016).

[87]C. H. Woo and B. N. Singh, "The concept of production bias and its possible role in defect accumulation under cascade damage conditions," Phys. Status Solidi B **159**, 609–616 (1990).
[88]C. H. Woo and B. N. Singh, "Production bias due to clustering of point defects in irradiation-induced cascades," Philos. Mag. A **65**, 889–912 (1992).
[89]C. H. Woo, B. N. Singh, and F. A. Garner, "Production bias: A proposed modification of the driving force for void swelling under cascade damage conditions," J. Nucl. Mater. **191–194**, 1224–1228 (1992).
[90]C. H. Woo, A. A. Semenov, and F. A. Garner, "Analysis of microstructural evolution driven by production bias," J. Nucl. Mater. **206**, 170–199 (1993).
[91]C. Domain, C. S. Becquart, and L. Malerba, "Simulation of radiation damage in Fe alloys: An object kinetic Monte Carlo approach," J. Nucl. Mater. **335**(1), 121–145 (2004).
[92]R. E. Stoller, S. I. Golubov, C. Domain, and C. S. Becquart, "Mean field rate theory and object kinetic Monte Carlo: A comparison of kinetic models," J. Nucl. Mater. **382**(2), 77–90 (2008).
[93]I. Rovelli, S. L. Dudarev, and A. P. Sutton, "Statistical model for diffusion-mediated recovery of dislocation and point-defect microstructure," Phys. Rev. E **98**, 043002 (2018).
[94]I. G. Margvelashvili and Z. K. Saralidze, "Influence of an elastic field of a dislocation on steady-state diffusion fluxes of point defects," Sov. Phys. Solid State **15**, 1774–1776 (1974).
[95]P. T. Heald, "The preferential trapping of interstitials at dislocations," Philos. Mag. **31**, 551–558 (1975).
[96]A. D. Brailsford and R. Bullough, "The theory of sink strengths," Philos. Trans. R. Soc. **302**, 87–137 (1981).
[97]M. J. Norgett, M. T. Robinson, and I. M. Torrens, "A proposed method of calculating displacement dose rates," Nucl. Eng. Des. **33**(1), 50–54 (1975).
[98]C. S. Becquart, C. Domain, A. Legris, and J. C. Van Duysen, "Influence of the interatomic potentials on molecular dynamics simulations of displacement cascades," J. Nucl. Mater. **280**(1), 73–85 (2000).
[99]K. Nordlund, S. Zinkle, A. E. Sand, F. Granberg, R. S. Averback, R. Stoller, T. Suzudo, L. Malerba, F. Banhart, W. Weber, F. Willaime, S. L. Dudarev, and D. Simeone, "Improving atomic displacement and replacement calculations with physically realistic damage models," Nat. Commun. **9**, 1048 (2018).
[100]K. Nordlund, S. Zinkle, A. E. Sand, F. Granberg, R. S. Averback, R. Stoller, T. Suzudo, L. Malerba, F. Banhart, W. Weber, F. Willaime, S. L. Dudarev, and D. Simeone, "Primary radiation damage: A review of current understanding and models," J. Nucl. Mater. **512**, 450–479 (2018).